Comparison of Somatic and Axonal Spike Shape Features in Cortical Neurons Grown on High-Density Microelectrode Arrays

Deligkaris Kosmas

Frey Initiative Research Unit

RIKEN Quantitative Biology Center

Osaka University

Graduate School of Frontier Biosciences

September 2015

Table of Contents

Table of Figures

Summary

Analysis of axonal spike shape and propagation properties can elucidate axonal mechanisms involved in learning and plasticity. Due to the thin diameter of the axon, analysis of axonal signals is technically challenging. Non-invasive extracellular recordings of axonal signals have small amplitudes, necessitating averaging of sub-threshold events. Here I present methods for analyzing axonal signals, and comparing them to somatic ones, based on a high-density microelectrode array (HDMEA), on which rat cortical neurons are grown. The HDMEA has 11,011 electrodes spaced densely enough to achieve sub-cellular resolution. I show that such a system can record large amplitude extracellular action potentials (EAPs) from both somata and axons. Areas devoid of neuronal somata showed electrical activity recorded by the HDMEA. The identified axonal spikes featured a variety of consistent waveforms and much shorter overall duration than somatic spikes. Under spontaneous activity conditions, both the amplitude and the duration of axonal EAPs were more resistant to changes induced by high-frequency activity than somatic EAPs. My findings have the following consequences: Firstly, they lay out frameworks for studies of axonal physiology, evidencing the contributions of axonal signals in overall HDMEA recordings and the differences in somatic and axonal waveshapes. Secondly, they reveal axonal firing characteristics of neurons embedded in an active network.

1. General Introduction

1.1. Generation and propagation of electrical signals in neurons

Neurons communicate by means of electrical and chemical signaling. When a neuron is active an electrical signal is generated at the axon hillock and then propagates to its axon terminals. This electrical signal is termed the action potential (AP). At the axon terminal, after the arrival of an AP, voltage-sensitive calcium channels open. The entrance of calcium in turn, causes the release of neurotransmitters into the synaptic gap, or cleft. Neurotransmitters are released into and diffuse at the synaptic cleft, reaching the terminals of the post-synaptic neuron. Ligand-gated ion channels at the post-synaptic neuron's membrane open, causing influx of charged ions and, potentially, generating a new AP in the post-synaptic neuron. The AP is an electrical signal, while synaptic communication is a chemical signal (Kandel et al., 2000). In this thesis, the focus is on the electrical form of communication, the AP.

The AP is generated at the axon initial segment, the distal part of axon hillock (Meeks and Mennerick, 2007; Shu et al., 2007a; Kole et al., 2007). It then follows two pathways, one down the axon and the other one back to the soma and dendrites. Traditionally, the axon has been thought of as an ideal transmission cable, a lossless cable whose function is to transmit information. However, recent experiments have shown that this assumption does not fully capture axonal behavior. Geiger and Jonas (Geiger and Jonas, 2000) have shown that high-frequency stimulation prolongs the duration of the axonal AP, up to three times. This in turn leads to larger calcium influx at the presynaptic terminal, potentiating the evoked excitatory response of the post-synaptic neuron. At branch points of spiny lobster motor neuron axonal propagation failures were observed at high frequency (>30 Hz) stimulation (Grossman et al., 1979a).

Such computational capacity of the axon may affect potential plasticity mechanisms and network activity. In neural schemes where the waveform shape of the AP is taken in account, a modification of the AP by the axon can alter the information coded. Dynamic changes in the axonal AP propagation can also prevent a network from over-excitation. For example, Meeks et al. (Meeks et al., 2005) have found two possible 'states' of axonal function. In one state, axonal spikes propagate reliably, whereas in the second state axonal spike propagation fails. Epileptiform activity, similar to plateau-potentials, or prolonged somatic depolarization induced the second state. Prolonged spiking without constant somatic depolarization resulted in faithful spike propagation.

The study by Meeks et al. was performed on acute hippocampal slices utilizing DC injection. Such acute slices do not form a complete network as they have been previously cut, but they provide a good model for investigating neuron-intrinsic properties. However, synaptic activity can shift such properties towards one or another regime (Magee, 2000; Spruston, 2008; Léger et al., 2005; Steriade, 2001). It would therefore be interesting to provide additional evidence about the reliability of axonal spike propagation in an active neuronal network. Such a network can be created by plating dissociated neurons and letting them develop *in-vitro*. After about one week *in-vitro* such networks exhibit spontaneous activity, much like the up/down states of the cortex (Corner, 2008; Van Pelt et al., 2004; Chiappalone et al., 2003). Such networks can be plated on microelectrode arrays (MEAs) and used for recordings.

1.2. Microelectrode arrays (MEAs) as a tool for axonal physiology

Overview of MEAs

An MEA is an array of substrate-integrated electrodes, typically allowing recording and stimulation of cells *in-vitro*. Electrode probes are also used for *in-vivo* experiments, tetrodes for example, but these are not considered here. The microelectrodes are typically made from inert conducting materials such as gold, platinum and ITO. A non-conductive layer is placed on top of the electrodes to limit electrode contact to the ionic medium. A glass or plastic ring is mounted in a way to form a chamber which can hold medium for electrophysiological experiments.

A first generation of MEAs (Gross et al., 1977; Pine, 1980; Thomas et al., 1972) consisted of 60-100 microelectrodes integrated on a glass substrate. These are passive MEAs since active circuitry (transistors, switches) is not found on chip. The fabrication of such devices allowed scientists to plate dissociated or organotypic cultures and record the extracellular electrical activity. Although dissociated neurons are easier to grow and experiment on, the *in-vivo* network architecture, and potentially other properties as well, is lost. Hundreds of thousands of dissociated cells are plated on MEAs, so the signals recorded by each of the 60 electrodes probably originates from multiple neurons. Because of such low spatial sampling, network-wide properties were mostly investigated (van Pelt et al., 2005; Chiappalone et al., 2006; Ito et al., 2010; Stegenga et al., 2008; Srinivas et al., 2007; Van Pelt et al., 2004). **Figure 1-1A** shows a conventional passive MEA as well as the neuron-electrode interface.

The fabrication of active, CMOS-based high-density MEAs (HDMEAs) with thousands of electrodes allowed experimentalists to record at higher spatial resolution. In combination with low-density cultures, recordings at single-neuron resolution might be possible. Such high spatial resolution recordings can aid in identifying activity-dependent mechanisms of single neurons.

A high-density MEA system, with an electrode density of 3,150 electrodes/mm^2 was presented by Frey et al. (Frey et al., 2010). Electrode diameter is 7 μm, while the electrode pitch is 18 μm. The HDMEA has 11,011 electrodes and 126 amplification channels. This means that at every point in time, a maximum of 126 electrodes can be used. However, the electrode configuration is flexible and can be changed in a matter of milliseconds. The extremely high density of electrodes makes the system ideal for use with low-density cultures. It further allows sub-cellular resolution recordings. This is the system used in the present work and is shown in **Figure 1-1B.**

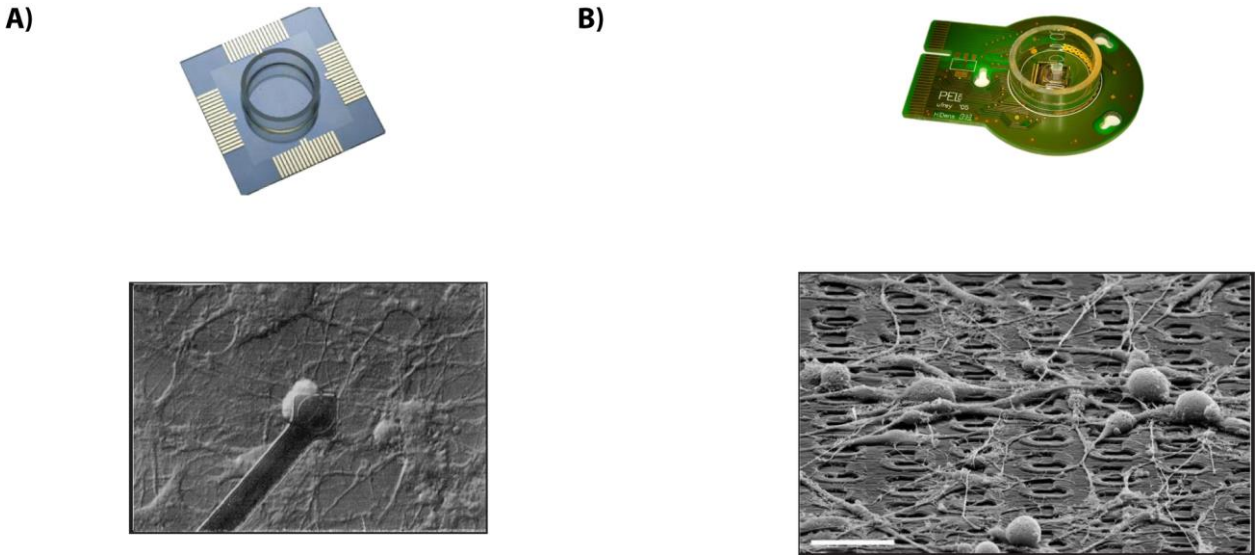

Figure 1-1. Illustration of passive and active MEAs. (A) Passive MEA and a zoom-in on the electrode array. On top of the electrode array, a neuronal network from dissociated hippocampal neurons can be seen. The electrode is the black dot. Taken from (Chiappalone et al., 2003) with permission. **(B)** CMOS HDMEA with 11,011 electrodes designed and fabricated by ETH Zurich. A scanning-electron microscope image of a zoom-in of the electrodes is shown with dorsal root ganglion neurons having being cultured on top. Scalebar 20 μm. Taken from (Frey et al., 2010) with permission.

Analyzing axonal electrophysiological properties with MEAs

A first study on axonal signals with the HDMEA has been presented by Bakkum et al. (Bakkum et al., 2013). The authors presented methods for tracking the stimulation-triggered axonal AP propagation in dissociated neurons. By electrically stimulating along the axonal arbor and subsequently averaging signals from multiple stimulation trials, the small-amplitude axonal signals became apparent and were subject to further analysis (**Figure 1-2A-B**). Axonal signals were characteristically bi- or tri-phasic with a prominent positive-first phase. Signal-to-noise ratios of $180*\sigma_{noise}$ for somatic and between 1 and $2*\sigma_{noise}$ for axonal signals were reported, necessitating the use of averaging for axonal signals (**Figure 1-2C-D**). Although a promising technique, there are cases where one needs to analyze individual spikes, rather than their average. For example, when analyzing activity-dependent changes based on the inter-spike interval. For this reason, an approach where axonal spikes are recorded at higher signal-to-noise ratio is needed.

Microtunnels as axonal amplifiers

A novel microfluidic platform was presented by Taylor et al. (Park et al., 2006; Taylor et al., 2005) for axonal physiology research. The system is composed of two compartments connected by narrow microtunnels (**Figure 1-3A**). By plating the cells in one side, the developing axons grow through the microtunnels and reach the other compartment (**Figure 1-3B**). Such a substrate isolates somata from axons and was found to be a good *in-vitro* model for axonal injury and regeneration studies. For example, Taylor et al. performed vacuum aspiration in the axonal

compartment to mimic axotomy, followed by collection of somata for further analysis (**Figure 1-3C**). Axonal regeneration was also studied by the application of neurotrophins on the axonal side.

Following the introduction of the microtunnel devices for axonal physiology studies, Dworak et al. (Dworak and Wheeler, 2009) applied this concept to MEA recordings. Microfluidic tunnels having a cross-section of 3x10 μm^2 were put on top of passive MEAs. By positioning the tunnels above the electrodes, axonal signals of large amplitude were recorded. Spikes with an amplitude of up to 4.5 mV were recorded in similar microtunnels by Pan et al. (Pan et al., 2014). **Figure 1-3D** shows an example of an MEA-microtunnel device. Lewandowska et al. established a protocol for microchannel recordings on the HDMEA (Lewandowska et al., 2015). The design is shown in **Figure 1-3E**, while the MAP2/Tau1/GFAP immunostained cells are shown in **Figure 1-3F**. It is interesting to note that also in this case axonal signals outside the wells were seen to be very small, tenths of μVs, while signals in microtunnels were in the order of hundreds of μVs (**Figure 1-3G**).

Unfortunately, the approach of MEA-microtunnels suffers from certain drawbacks that need to be further investigated. Firstly, the axons are in a constraint environment. The limited space inside the microtunnels might result in axonal overcrowding. Bastmeyer et al. observed both thickening and thinning of axon shafts in corticospinal axons (Bastmeyer and O'Leary, 1996). Such variation in axonal thickness in a crowded environment will result in a similar change in compressive forces by the microtunnels. Previously-severed, regenerating fibers, growing through polyimide sieve electrodes, showed an increase in axonal diameter during regeneration, with some showing signs of compressive axonopathy (Lago et al., 2005).

Secondly, immunostaining experiments suffer from reduced diffusion of molecules caused by the narrow microchannels (Lewandowska et al., 2015). Besides, uncrosslinked PDMS can diffuse out of the PDMS bulk, while PDMS might absorb serum components (Regehr et al., 2009), altering the extracellular environment. In the microchannel designs shown in **Figure 1-3** the somata are in open-wells while the axons are inside the microtunnels. The medium volume contained in the microchannels might suffer from more component-depletion than the medium volume in the open wells.

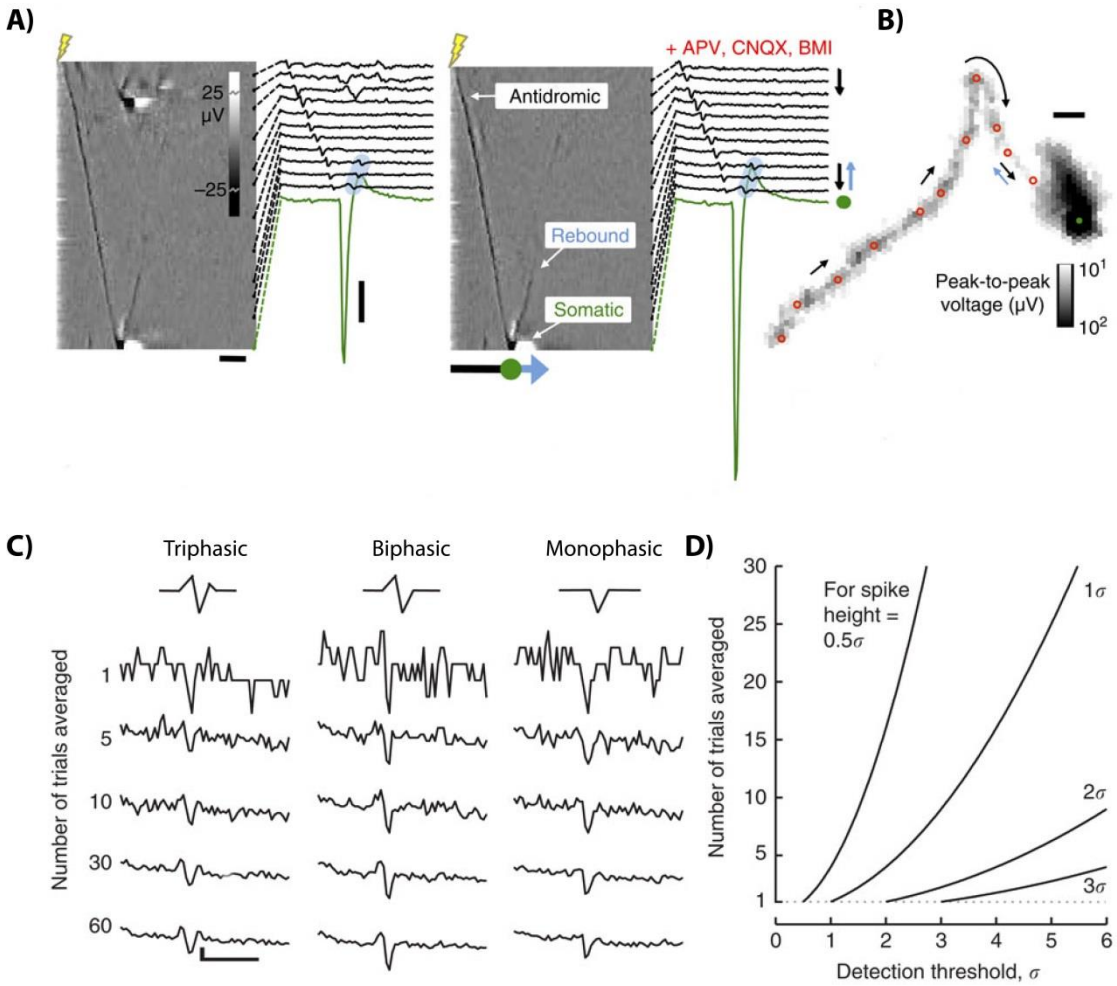

Figure 1-2. Axonal spike propagation recorded by the HDMEA. (A) Sixty stimulation trials were performed and resulting signals were averaged. The mean voltages are shown here for standard culture media (left) and for culture media supplemented with the synaptic receptor antagonists 2-amino-5-phosphonovaleric acid (APV), CNQX and bicuculline methiodide. The heatmaps show the site of electrical stimulation (yellow bolts), the subsequent axonal pathway (dark line), the somatic depolarization following the antidromic axonal action potential (green signal), and an action potential rebounding from the soma (blue). The propagation direction is indicated by arrows. **(B)** Tracing of the axonal pathway in **(A)**, generated by 17 adjacent recordings. Scalebar 100 µm. **(C)** Axonal spike shapes recorded after stimulation. Three types are shown: triphasic, biphasic, monophasic. The top row shows individual traces. The bottom rows show the resulting traces after averaging. Scalebars 1 ms horizontal, 10 µV vertical. **(D)** Common spike-detection algorithms are based on a threshold crossing detection. Here shown is the number of trials needed to detect a spike with a given height (0.5-3σ) with respect to the detection threshold. A common threshold for spike detection is 5σ. Taken from (Bakkum et al., 2013) with permission.

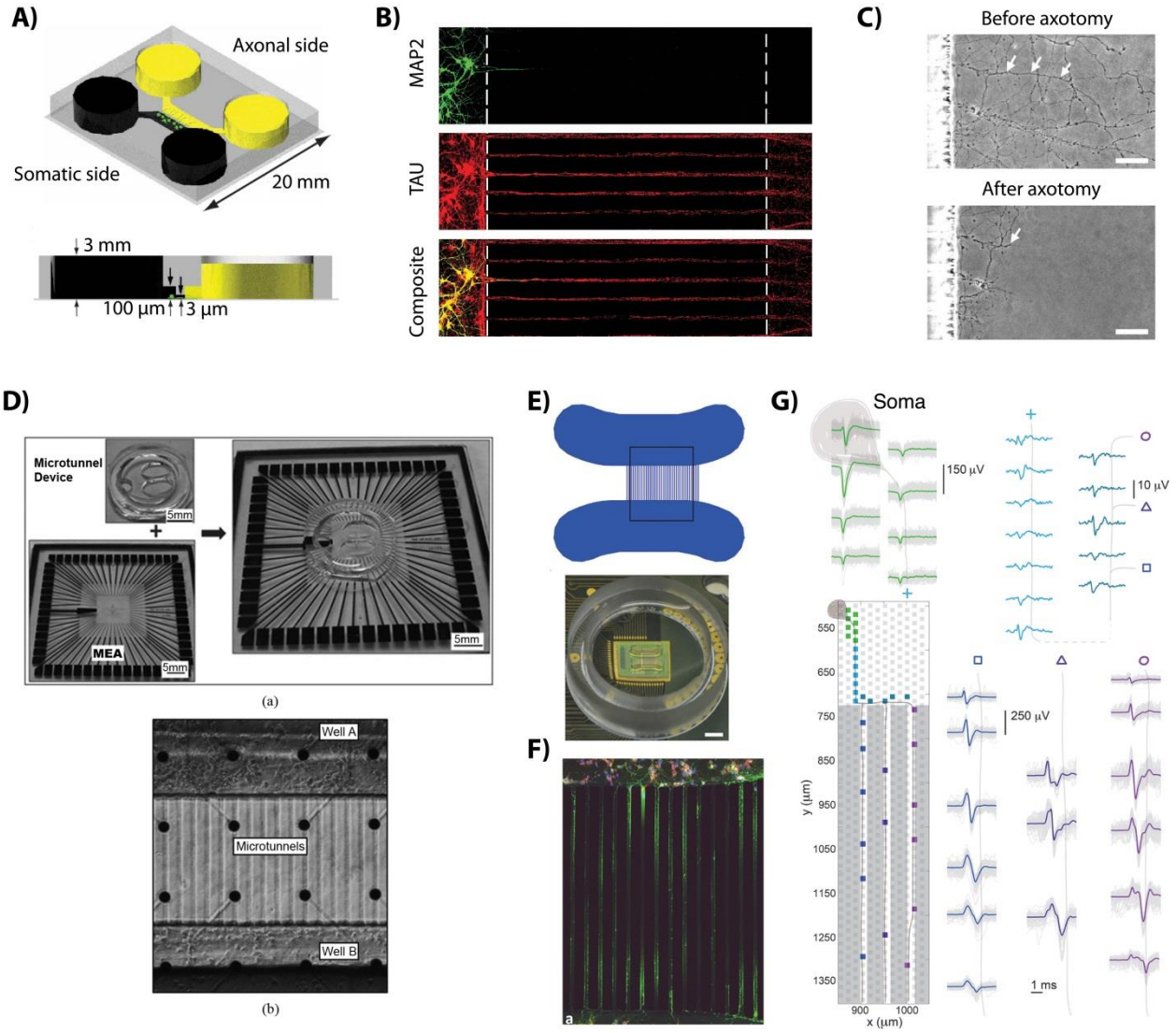

Figure 1-3. Microtunnels and their applications to MEA recordings. (A) Schematic of the original microchannel device where two compartments, one somatic and one axonal, are connected with microchannels. Black side is the somatic side, yellow side is the axonal side. **(B).** Immunostaining in the system shown in **(A)** indicated that only axons grow through the tunnels. Lack of prominent MAP2 staining indicates absence of dendrites, while the size of the microtunnels physically blocks the somata to enter. **(C)** Axotomy studies facilitated by the system shown in **(A)**. By using vacuum aspiration researchers were able to mimick axotomy in the open-well axonal side. Scale bars 50 µm. **(D)** Implementation of the microchannel concept on a passive MEA. Both wells are plated with neurons which grow neurites through the microtunnels. Electrodes below the microtunnels can record axonal spikes. **(E)** Design of the microchannel device in use with the HDMEA system. Similar to **(D),** two chambers are flooded with cells. Neurites then grow through the microtunnels, connecting the two compartments. **(F)** Immunostaining showed that only axons pass through the microtunnels in the HDMEA. Note reduced staining at the center of the tunnels. Composite image: MAP2 (soma and dendrites) is shown in purple, Tau1 (axons) in green, DAPI (nuclei) in blue, GFAP (glia) in red. **(G)** Axonal spikes inside microtunnels are larger than axonal spikes outside the tunnels. A cartoon neuron is shown in the upper left side for guidance. The signal can be traced from the soma to the three vertical, parallel microchannels. The color of the square electrodes corresponds to the color of the spikes shown. It can be seen that the axonal spikes inside microtunnels (purple, dark blue) is around 250 µV, whereas outside the microtunnels are in the order of 10 µV. **(A)-(C)** Taken from (Taylor et al., 2005) with permission, **(D)** Taken from (Pan et al., 2014) with permission, **(E)-(G)** Taken from (Lewandowska et al., 2015) with permission.

1.3. Summary & formulation of research direction

Section 1.1 described the need to characterize axonal and somatic properties in active networks. Section 1.2 gave a brief introduction on MEAs and how they can potentially be used in axonal physiology studies. The major advantage of MEAs is the non-invasive nature of the technique, as well as the long-term possibility of recordings from the same neuron. With the advent of HDMEAs new possibilities have opened. The specifications of active MEAs are still improving, with the fabrication and successful application of a 26,400-electrodes/1024-amplification channels HDMEA recently published (Müller et al., 2015). The major disadvantage of extracellular measurements for axonal physiology is the small amplitude of axonal signals However, due to being a relatively young technique, the full potential of HDMEAs has not been fully explored yet. In addition, the exact biophysical origin of the extracellular recordings, and the reasons for their variability are still relatively unknown (Anastassiou et al., 2015).

This project is focused on two goals. Firstly, to further explore the quality of axonal signal recordings, utilizing beta-III-tubulin immunostaining and electrophysiological recordings from all 11,011 electrodes. Such an approach will also provide experimental evidence for the sources of non-somatic electrical activity in HDMEA recordings, and help elucidate the origin of different spike shapes (Nam and Wheeler, 2011). Secondly, to characterize differences and similarities of axonal and somatic signals in the spontaneous activity of neural networks.

2. References

Anastassiou, C. a., Perin, R., Buzsaki, G., Markram, H., and Koch, C. (2015). *Cell-type- and activity-dependent extracellular correlates of intracellular spiking*. doi:10.1152/jn.00628.2014.

Bakkum, D. J., Frey, U., Radivojevic, M., Russell, T. L., Müller, J., Fiscella, M., Takahashi, H., and Hierlemann, A. (2013). Tracking axonal action potential propagation on a high-density microelectrode array across hundreds of sites. *Nat. Commun.* 4, 2181. doi:10.1038/ncomms3181.

Baltz, T., de Lima, A. D., and Voigt, T. (2010). Contribution of GABAergic interneurons to the development of spontaneous activity patterns in cultured neocortical networks. *Front. Cell. Neurosci.* 4, 15. doi:10.3389/fncel.2010.00015.

Barthó, P., Hirase, H., Monconduit, L., Zugaro, M., Harris, K. D., and Buzsáki, G. (2004). Characterization of neocortical principal cells and interneurons by network interactions and extracellular features. *J. Neurophysiol.* 92, 600–8. doi:10.1152/jn.01170.2003.

Bastmeyer, M., and O'Leary, D. D. (1996). Dynamics of target recognition by interstitial axon branching along developing cortical axons. *J. Neurosci.* 16, 1450–1459.

Becchetti, A., Gullo, F., Bruno, G., Dossi, E., Lecchi, M., and Wanke, E. (2012). Exact distinction of excitatory and inhibitory neurons in neural networks: a study with GFP-GAD67 neurons optically and electrophysiologically recognized on multielectrode arrays. *Front. Neural Circuits* 6, 63. doi:10.3389/fncir.2012.00063.

Beggs, J. M., and Plenz, D. (2003). Neuronal avalanches in neocortical circuits. *J. Neurosci.* 23, 11167–77. Available at: http://www.ncbi.nlm.nih.gov/pubmed/14657176.

Berdondini, L., Massobrio, P., Chiappalone, M., Tedesco, M., Imfeld, K., Maccione, A., Gandolfo, M., Koudelka-Hep, M., and Martinoia, S. (2009). Extracellular recordings from locally dense microelectrode arrays coupled to dissociated cortical cultures. *J. Neurosci. Methods* 177, 386–396. doi:10.1016/j.jneumeth.2008.10.032.

Blanche, T. J., and Swindale, N. V (2006). Nyquist interpolation improves neuron yield in multiunit recordings. *J. Neurosci. Methods* 155, 81–91. doi:10.1016/j.jneumeth.2005.12.031.

Chance, F. S., Abbott, L. F., and Reyes, A. D. (2002). Gain modulation from background synaptic input. *Neuron* 35, 773–782. doi:10.1016/S0896-6273(02)00820-6.

Chiappalone, M., Bove, M., Vato, A., Tedesco, M., and Martinoia, S. (2006). Dissociated cortical networks show spontaneously correlated activity patterns during in vitro development. *Brain Res.* 1093, 41–53. doi:10.1016/j.brainres.2006.03.049.

Chiappalone, M., Vato, A., Tedesco, M. B., Marcoli, M., Davide, F., and Martinoia, S. (2003). Networks of neurons coupled to microelectrode arrays: a neuronal sensory system for pharmacological applications. *Biosens. Bioelectron.* 18, 627–634.

Claverol-Tinture, E., and Pine, J. (2002). Extracellular potentials in low-density dissociated neuronal cultures. *J. Neurosci. Meth.* 117, 13–21.

Corner, M. a. (2008). Spontaneous neuronal burst discharges as dependent and independent variables in the maturation of cerebral cortex tissue cultured in vitro: A review of activity-dependent studies in live “model” systems for the development of intrinsically generated bioel. *Brain Res. Rev.* 59, 221–244. doi:10.1016/j.brainresrev.2008.08.001.

Czarnecki, A., Tscherter, A., and Streit, J. (2012). Network activity and spike discharge oscillations in cortical slice cultures from neonatal rat. *Eur. J. Neurosci.* 35, 375–388. doi:10.1111/j.1460-9568.2011.07966.x.

Debanne, D. (2004). Information processing in the axon. *Nat. Rev. Neurosci.* 5, 304–316. doi:10.1038/nrn1397.

Debanne, D., Campanac, E., Bialowas, A., Carlier, E., and Alcaraz, G. (2011). Axon physiology. *Physiol. Rev.* 91, 555–602. doi:10.1152/physrev.00048.2009.

Destexhe, a, and Paré, D. (1999). Impact of network activity on the integrative properties of neocortical pyramidal neurons in vivo. *J. Neurophysiol.* 81, 1531–1547.

Dworak, B. J., and Wheeler, B. C. (2009). Novel MEA platform with PDMS microtunnels enables the detection of action potential propagation from isolated axons in culture. *Lab Chip* 9, 404–10. doi:10.1039/b806689b.

Le Feber, J., Stegenga, J., and Rutten, W. L. C. (2010). The effect of slow electrical stimuli to achieve learning in cultured networks of rat cortical neurons. *PLoS One* 5, e8871. doi:10.1371/journal.pone.0008871.

Fiscella, M., Farrow, K., Jones, I. L., Jäckel, D., Müller, J., Frey, U., Bakkum, D. J., Hantz, P., Roska, B., and Hierlemann, A. (2012). Recording from defined populations of retinal ganglion cells using a high-density CMOS-integrated microelectrode array with real-time switchable electrode selection. *J. Neurosci. Methods* 211, 103–13. doi:10.1016/j.jneumeth.2012.08.017.

Fitzgerald, J. J., Lacour, S. P., McMahon, S. B., and Fawcett, J. W. (2008). Microchannels as axonal amplifiers. *IEEE Trans. Biomed. Eng.* 55, 1136–46. doi:10.1109/TBME.2007.909533.

Frey, U., Sedivy, J., Heer, F., Pedron, R., Ballini, M., Mueller, J., Bakkum, D., Hafizovic, S., Faraci, F. D., Greve, F., et al. (2010). Switch-Matrix-Based High-Density Microelectrode Array in CMOS Technology. *Solid-State Circuits, IEEE J.* 45, 467–482. doi:10.1109/JSSC.2009.2035196.

Furukawa, Y., Kasai, N., and Torimitsu, K. (2009). Effect of Mg2+ on neural activity of rat cortical and hippocampal neurons in vitro. *Magnes. Res.* 22, 174S–181S. Available at: http://www.ncbi.nlm.nih.gov/pubmed/19780405.

Geiger, R. P., and Jonas, P. (2000). Dynamic Control of Presynaptic Ca2+ Inflow by Fast-Inactivating K+ Channels in Hippocampal Mossy Fiber Boutons. *Neuron* 28, 927–939. doi:10.1016/S0896-6273(00)00164-1.

Golding, N. L., and Spruston, N. (1998). Dendritic sodium spikes are variable triggers of axonal action potentials in hippocampal CA1 pyramidal neurons. *Neuron* 21, 1189–1200. doi:10.1016/S0896-6273(00)80635-2.

Gritsun, T. a, le Feber, J., and Rutten, W. L. C. (2012). Growth dynamics explain the development of spatiotemporal burst activity of young cultured neuronal networks in detail. *PLoS One* 7, e43352. doi:10.1371/journal.pone.0043352.

Gross, G., Rieske, E., Kreutzberg, G., and Meyer, A. (1977). A new fixed-array multi-microelectrode system designed for long-term monitoring of extracellular single unit neuronal activity in vitro. *Neurosci. Lett.* 6, 101–105. Available at: http://linkinghub.elsevier.com/retrieve/pii/0304394077900039 [Accessed February 1, 2011].

Grossman, Y., Parnas, I., and Spira, M. E. (1979a). Differential conduction block in branches of a bifurcating axon. *J. Physiol.* 295, 283–305.

Grossman, Y., Parnas, I., and Spira, M. E. (1979b). Mechanisms involved in differential conduction of potentials at high frequency in a branching axon. *J. Physiol.* 295, 307–322.

Grubb, M. S., and Burrone, J. (2010). Activity-dependent relocation of the axon initial segment fine-tunes neuronal excitability. *Nature* 465, 1070–4. doi:10.1038/nature09160.

Henze, D. A., Borhegyi, Z., Csicsvari, J., Mamiya, A., Harris, K. D., and Buzsáki, G. (2000). Intracellular features predicted by extracellular recordings in the hippocampus in vivo. *J.*

Neurophysiol. 84, 390–400. Available at: http://jn.physiology.org/cgi/content/abstract/84/1/390 [Accessed December 11, 2014].

Hill, D. N., Mehta, S. B., and Kleinfeld, D. (2011). Quality metrics to accompany spike sorting of extracellular signals. *J. Neurosci.* 31, 8699–705. doi:10.1523/JNEUROSCI.0971-11.2011.

Huguenard, J. R., Hamill, O. P., and Prince, D. a (1989). Sodium channels in dendrites of rat cortical pyramidal neurons. *Proc. Natl. Acad. Sci. U. S. A.* 86, 2473–2477.

Ito, D., Tamate, H., Nagayama, M., Uchida, T., Kudoh, S. N., and Gohara, K. (2010). Minimum neuron density for synchronized bursts in a rat cortical culture on multi-electrode arrays. *Neuroscience* 171, 50–61. doi:10.1016/j.neuroscience.2010.08.038.

Jäckel, D., Frey, U., Fiscella, M., Franke, F., and Hierlemann, A. (2012). Applicability of independent component analysis on high-density microelectrode array recordings. *J. Neurophysiol.* 108, 334–48. doi:10.1152/jn.01106.2011.

Jensen, C. S., Rasmussen, H. B., and Misonou, H. (2011). Neuronal trafficking of voltage-gated potassium channels. *Mol. Cell. Neurosci.* 48, 288–297. doi:10.1016/j.mcn.2011.05.007.

Kandel, E. R., Schwartz, J. H., and Jessell, T. M. (2000). *Principles of Neural Science*. doi:10.1036/0838577016.

Khodagholy, D., Gelinas, J. N., Thesen, T., Doyle, W., Devinsky, O., Malliaras, G. G., and Buzsáki, G. (2014). NeuroGrid : recording action potentials from the surface of the brain. *Nat. Neurosci.* doi:10.1038/nn.3905.

Kole, M. H. P., Ilschner, S. U., Kampa, B. M., Williams, S. R., Ruben, P. C., and Stuart, G. J. (2008). Action potential generation requires a high sodium channel density in the axon initial segment. *Nat. Neurosci.* 11, 178–186. doi:10.1038/nn2040.

Kole, M. H. P., Letzkus, J. J., and Stuart, G. J. (2007). Axon Initial Segment Kv1 Channels Control Axonal Action Potential Waveform and Synaptic Efficacy. *Neuron* 55, 633–647. doi:10.1016/j.neuron.2007.07.031.

Lago, N., Ceballos, D., J Rodríguez, F., Stieglitz, T., and Navarro, X. (2005). Long term assessment of axonal regeneration through polyimide regenerative electrodes to interface the peripheral nerve. *Biomaterials* 26, 2021–2031. doi:10.1016/j.biomaterials.2004.06.025.

Léger, J., Stern, E., Aertsen, A., and Heck, D. (2005). Synaptic integration in rat frontal cortex shaped by network activity. *J. Neurophysiol.* 93, 281–293. doi:10.1152/jn.00067.2003.

Lewandowska, M. K., Bakkum, D. J., Rompani, S. B., and Hierlemann, A. (2015). Recording Large Extracellular Spikes in Microchannels along Many Axonal Sites from Individual Neurons. *PLoS One* 10, e0118514. doi:10.1371/journal.pone.0118514.

Maccione, A., Benfenati, F., Berdondini, L., Gandolfo, M., Tedesco, M., Martinoia, S., Imfeld, K., and Koudelka-Hep, M. (2009). Imaging extracellular neuronal signaling on high resolution microelectrode arrays (MEAs): hippocampal cultures coupled with a high resolution neuroelectronic interface. *2009 4th Int. IEEE/EMBS Conf. Neural Eng. (NER 2009)*, 234–7|753. doi:10.1109/ner.2009.5109276.

Magee, J. C. (2000). Dendritic integration of excitatory synaptic input. *Nat. Rev. Neurosci.* 1, 181–190. doi:10.1038/35044552.

Meeks, J. P., Jiang, X., and Mennerick, S. (2005). Action potential fidelity during normal and epileptiform activity in paired soma-axon recordings from rat hippocampus. *J. Physiol.* 566, 425–441. doi:10.1113/jphysiol.2005.089086.

Meeks, J. P., and Mennerick, S. (2007). Action potential initiation and propagation in CA3 pyramidal axons. *J. Neurophysiol.* 97, 3460–3472. doi:10.1152/jn.01288.2006.

Mickus, T., Jung, H., and Spruston, N. (1999). Properties of Slow, Cumulative Sodium Channel Inactivation in Rat Hippocampal CA1 Pyramidal Neurons. 76, 846–860.

Monsivais, P., Clark, B. A., Roth, A., and Hausser, M. (2005). Determinants of action potential propagation in cerebellar Purkinje cell axons. *J Neurosci* 25, 464–472. Available at: http://eutils.ncbi.nlm.nih.gov/entrez/eutils/elink.fcgi?cmd=prlinks&dbfrom=pubmed&retmode=ref&id=15647490.

Müller, J., Ballini, M., Livi, P., Chen, Y., Radivojevic, M., Shadmani, A., Viswam, V., Jones, I. L., Fiscella, M., Diggelmann, R., et al. (2015). High-resolution CMOS MEA platform to study neurons at subcellular, cellular, and network levels. *Lab Chip*. doi:10.1039/C5LC00133A.

Nam, Y., and Wheeler, B. C. (2011). In vitro microelectrode array technology and neural recordings. *Crit. Rev. Biomed. Eng.* 39, 45–61. Available at: http://www.ncbi.nlm.nih.gov/pubmed/21488814.

Opitz, T., De Lima, A. D., and Voigt, T. (2002). Spontaneous development of synchronous oscillatory activity during maturation of cortical networks in vitro. *J. Neurophysiol.* 88, 2196–206. doi:10.1152/jn.00316.2002.

Pan, L., Alagapan, S., Franca, E., Demarse, T., Brewer, G. J., and Wheeler, B. C. (2014). Large extracellular spikes recordable from axons in microtunnels. *IEEE Trans. Neural Syst. Rehabil. Eng.* 22, 453–459. doi:10.1109/TNSRE.2013.2289911.

Paré, D., Shink, E., Gaudreau, H., Destexhe, a, and Lang, E. J. (1998). Impact of spontaneous synaptic activity on the resting properties of cat neocortical pyramidal neurons In vivo. *J. Neurophysiol.* 79, 1450–1460.

Park, J. W., Vahidi, B., Taylor, A. M., Rhee, S. W., and Jeon, N. L. (2006). Microfluidic culture platform for neuroscience research. *Nat. Protoc.* 1, 2128–36. doi:10.1038/nprot.2006.316.

Van Pelt, J., Corner, M. a, Wolters, P. S., Rutten, W. L. C., and Ramakers, G. J. a (2004). Longterm stability and developmental changes in spontaneous network burst firing patterns in dissociated rat cerebral cortex cell cultures on multielectrode arrays. *Neurosci. Lett.* 361, 86–9. doi:10.1016/j.neulet.2003.12.062.

Van Pelt, J., Vajda, I., Wolters, P. S., Corner, M. a, and Ramakers, G. J. a (2005). Dynamics and plasticity in developing neuronal networks in vitro. *Prog. Brain Res.* 147, 173–88. doi:10.1016/S0079-6123(04)47013-7.

Pine, J. (1980). Recording action potentials from cultured neurons with extracellular microcircuit electrodes. *J. Neurosci. Methods* 2, 19–31. Available at: http://linkinghub.elsevier.com/retrieve/pii/0165027080900424 [Accessed February 1, 2011].

Regehr, K. J., Domenech, M., Koepsel, J. T., Carver, K. C., Ellison-Zelski, S. J., Murphy, W. L., Schuler, L. a, Alarid, E. T., and Beebe, D. J. (2009). Biological implications of polydimethylsiloxane-based microfluidic cell culture. *Lab Chip* 9, 2132–2139. doi:10.1039/b903043c.

Rivera, J., Chu, P. J., Lewis, T. L., and Arnold, D. B. (2007). The role of Kif5B in axonal localization of Kv1 K+ channels. *Eur. J. Neurosci.* 25, 136–146. doi:10.1111/j.1460-9568.2006.05277.x.

Robbins, A. a, Fox, S. E., Holmes, G. L., Scott, R. C., and Barry, J. M. (2013). Short duration waveforms recorded extracellularly from freely moving rats are representative of axonal activity. *Front. Neural Circuits* 7, 181. doi:10.3389/fncir.2013.00181.

Scott, L. L., Hage, T. a, and Golding, N. L. (2007). Weak action potential backpropagation is associated with high-frequency axonal firing capability in principal neurons of the gerbil medial superior olive. *J. Physiol.* 583, 647–661. doi:10.1113/jphysiol.2007.136366.

Shibata, R., Nakahira, K., Shibasaki, K., Wakazono, Y., Imoto, K., and Ikenaka, K. (2000). A-type K+ current mediated by the Kv4 channel regulates the generation of action potential in developing cerebellar granule cells. *J. Neurosci.* 20, 4145–4155. doi:20/11/4145 [pii].

Shu, Y., Duque, A., Yu, Y., Haider, B., and McCormick, D. a (2007a). Properties of action-potential initiation in neocortical pyramidal cells: evidence from whole cell axon recordings. *J. Neurophysiol.* 97, 746–60. doi:10.1152/jn.00922.2006.

Shu, Y., Yu, Y., Yang, J., and McCormick, D. a (2007b). Selective control of cortical axonal spikes by a slowly inactivating K+ current. *Proc. Natl. Acad. Sci. U. S. A.* 104, 11453–11458. doi:10.1073/pnas.0702041104.

Spruston, N. (2008). Pyramidal neurons: dendritic structure and synaptic integration. *Nat. Rev. Neurosci.* 9, 206–21. doi:10.1038/nrn2286.

Srinivas, K. V, Jain, R., Saurav, S., and Sikdar, S. K. (2007). Small-world network topology of hippocampal neuronal network is lost, in an in vitro glutamate injury model of epilepsy. *Eur. J. Neurosci.* 25, 3276–86. doi:10.1111/j.1460-9568.2007.05559.x.

Stegenga, J., Le Feber, J., Marani, E., and Rutten, W. L. C. (2008). Analysis of cultured neuronal networks using intraburst firing characteristics. *IEEE Trans. Biomed. Eng.* 55, 1382–90. doi:10.1109/TBME.2007.913987.

Steriade, M. (2001). Impact of network activities on neuronal properties in corticothalamic systems. *J. Neurophysiol.* 86, 1–39.

Stratton, P., Cheung, A., Wiles, J., Kiyatkin, E., Sah, P., and Windels, F. (2012). Action potential waveform variability limits multi-unit separation in freely behaving rats. *PLoS One* 7. doi:10.1371/journal.pone.0038482.

Stutzki, H., Leibig, C., Andreadaki, A., Fischer, D., and Zeck, G. (2014). Inflammatory stimulation preserves physiological properties of retinal ganglion cells after optic nerve injury. *Front. Cell. Neurosci.* 8, 38. doi:10.3389/fncel.2014.00038.

Sun, J.-J., Kilb, W., and Luhmann, H. J. (2010). Self-organization of repetitive spike patterns in developing neuronal networks in vitro. *Eur. J. Neurosci.* 32, 1289–99. doi:10.1111/j.1460-9568.2010.07383.x.

Taylor, A. M., Blurton-Jones, M., Rhee, S. W., Cribbs, D. H., Cotman, C. W., and Jeon, N. L. (2005). A microfluidic culture platform for CNS axonal injury, regeneration and transport. *Nat. Methods* 2, 599–605. doi:10.1038/nmeth777.

Thomas, C. A., Springer, P. A., Loeb, G. E., Berwald-Netter, Y., and Okum, L. M. (1972). A miniature microelectrode array to monitor the bioelectric activity of cultured cells. *Exp. Cell Res.* 74, 61–66.

Ullo, S., Nieus, T. R., Sona, D., Maccione, A., Berdondini, L., and Murino, V. (2014). Functional connectivity estimation over large networks at cellular resolution based on electrophysiological recordings and structural prior. *Front. Neuroanat.* 8, 137. doi:10.3389/fnana.2014.00137.

Weihberger, O., Okujeni, S., Mikkonen, J. E., and Egert, U. (2013). Quantitative examination of stimulus-response relations in cortical networks in vitro. *J. Neurophysiol.* 109, 1764–74. doi:10.1152/jn.00481.2012.

Weir, K., Blanquie, O., Kilb, W., Luhmann, H. J., and Sinning, A. (2015). Comparison of spike parameters from optically identified GABAergic and glutamatergic neurons in sparse cortical cultures. *Front. Cell. Neurosci.* 8, 1–12. doi:10.3389/fncel.2014.00460.

Zeck, G., Lambacher, A., and Fromherz, P. (2011). Axonal transmission in the retina introduces a small dispersion of relative timing in the ganglion cell population response. *PLoS One* 6, e20810. doi:10.1371/journal.pone.0020810.

3. Introduction

Action potentials (APs) are short, self-sustaining voltage transients observed in excitable membranes of several cell types. In neurons these so called “spikes” have been observed in the dendrite, the soma and in the axon. APs are generated at the axon initial segment (Meeks and Mennerick, 2007; Shu et al., 2007a; Kole et al., 2007) and transmitted through the axon arbor to the synapses. The axon itself is not an ideal transmission cable (Debanne et al., 2011). Axonal conduction failures (Monsivais et al., 2005; Grossman et al., 1979b) and AP widening (Geiger and Jonas, 2000) can affect downstream synaptic communication. Axonal AP characteristics are, therefore, important for communication and plasticity.

A previous study in acute hippocampal slices has shown that axonal spikes exhibited significant amplitude reduction during long-lasting plateau-potentials (PPs), induced by short-duration somatic depolarizing current pulses (Meeks et al., 2005). Recurrent somatic depolarizations did not result in such axonal spike amplitude reduction. Furthermore, late spikes during PPs failed to propagate, indicating that the reliability of axonal spike propagation correlates with the depolarization state of the soma.

The depolarization state of the soma, in-turn, can be influenced by network activity. The spatial and temporal summation of excitatory and inhibitory synaptic inputs induces somatic membrane voltage fluctuations (Magee, 2000; Spruston, 2008). Such synaptic integration can be modulated by the background network activity (Léger et al., 2005; Paré et al., 1998; Steriade, 2001; Destexhe and Paré, 1999; Chance et al., 2002). In organotypic and dissociated cultures, network activity is retained, and such cultures exhibit global synchronous oscillations or bursts (Ito et al., 2010; Czarnecki et al., 2012; Van Pelt et al., 2004; Chiappalone et al., 2006; Beggs and Plenz, 2003; Baltz et al., 2010). Bursts are very similar to UP states, during which the soma is at a depolarized potential. In contrast to acute slices, *in-vitro* developing networks provide a good experimental model for assessing electrophysiological properties of neurons embedded in an active network.

Dissociated or organotypic cultures can be grown on microelectrode arrays (MEAs), providing an experimental set-up for analysis of spontaneous activity. After their introduction (Gross et al., 1977; Pine, 1980; Thomas et al., 1972) MEAs were, e.g., used for neural network analysis including network maturation (Opitz, De Lima, and Voigt 2002; J Van Pelt et al. 2004; Jaap van Pelt et al. 2005), oscillatory activity in normal and pathological states (Srinivas et al., 2007), effects of electrical stimulation (le Feber et al., 2010; Weihberger et al., 2013), pharmacology (Furukawa et al., 2009), and the role of specific neuronal subtypes in rhythmic oscillations (Baltz et al., 2010), among others. However, despite the huge amount of work, the exact origin of the various extracellular spike shapes is still incompletely understood.

The availability of active, complementary-metal-oxide-semiconductor (CMOS) based high-density MEAs (HDMEAs) with thousands of electrodes allows experimentalists to record at higher spatial resolution (Berdondini et al., 2009; Maccione et al., 2009; Fiscella et al., 2012; Jäckel et al., 2012; Bakkum et al., 2013; Stutzki et al., 2014). It was shown that HDMEAs enable non-invasive somatic and axonal extracellular recordings from neurons embedded in an active network. Bakkum et al. showed a procedure to track axonal signal propagation on an HDMEA by averaging responses to electrical stimulation (Bakkum et al., 2013). Axonal signals are generally

small (around 10 µV amplitude), which requires averaging of several of them to image the full length of an axonal arbor.

In order to increase the amplitude of the extracellularly measured axonal spikes, polydimethylsiloxane (PDMS) microtunnels can be used in combination with MEAs. Such microchannel structures were introduced by Taylor et al. (Taylor et al., 2005) on glass slides and later developed for passive (Dworak and Wheeler, 2009; Pan et al., 2014) and HDMEAs (Lewandowska et al., 2015). These are long, narrow tunnels through which only axons can pass. The small extracellular space in such tunnels results in increased sealing resistance and larger spike amplitudes (Fitzgerald et al., 2008). Axonal microtunnels provide very high signal amplification, up to 20-150 times compared to open-well signals (Pan et al., 2014; Lewandowska et al., 2015). However, PDMS microtunnels may have certain disadvantages. For example, Bastmeyer et al. observed both thickening and thinning of axon shafts in corticospinal axons (Bastmeyer and O'Leary, 1996). Such variation in axonal thickness in a restricted and crowded environment may produce corresponding compressive forces inside the microtunnels. Moreover, uncrosslinked PDMS components may diffuse out of the PDMS bulk, while PDMS might absorb serum components (Regehr et al., 2009), altering the local axonal extracellular environment.

In view of the issues described above I decided to conduct axonal physiology experiments in open-well cultures. I searched for the sources of the electrical activity by combining electrophysiological recordings and post-hoc immunofluorescence imaging. Our results suggest that not only individual somatic, but also neuritic spikes can be detected by a threshold-detector. These neurites were immunopositive for β3-tubulin. Adaptation properties of these neuritic spikes, as well as other supportive evidence, favor an axonal over a dendritic identity. The duration of axonal spikes was, on average much narrower than somatic spikes.

4. Materials and methods

4.1. Animals

Timed pregnant rats (Wistar) were obtained from a commercial vendor (Nihon SLC). Animals were sacrificed on the day of arrival to obtain embryos for primary neuron cultures. All experimental procedures on animals were carried out in accordance with the European Council Directive of 22 September 2010 (2010/63/EU) and had been approved by the local authorities (Animal Care and Use Committee of RIKEN; QAH24-01).

4.2. Primary neuron culture

Cultures were prepared according to a previously published protocol (Bakkum et al., 2013) with minor modifications. Briefly, timed-pregnant Wistar rats were anesthetized with Isofluorane and sacrificed with a sharp-blade guillotine. The embryos (embryonal day 16-18) were extracted and euthanized by spinal cord bisection. Their brains were quickly removed and placed in ice-cold dissection medium (Table S1). Cortices from 2-3 embryos were pooled for one plating. The cortices were isolated and enzymatically dissociated in 0.25% Trypsin with ethylene-diamine-tetra-acetate (EDTA) for 20 minutes in a warm water bath (37°C). Cortices were washed twice for one minute with plating medium. The tissue was mechanically triturated with a P1000 (Gilson) pipette. The cell solution was filtered through a 40 μm filter to remove aggregates and then centrifuged at 1100 rpm for 6 minutes. The supernatant was removed leaving 1-2 ml of the cell pellet solution. The cells were counted and diluted to the appropriate density. 5000 or 10000 cells were plated on the HDMEA (see below) in a 20 μl drop centered on the electrode area. Cultures were then placed in the preservation incubator. After waiting 30 minutes for the cells to attach, the HDMEA chambers were slowly filled with 900 μl of plating medium. Three days later the medium was changed for the first time by completely replacing it with growth medium. Afterwards, 30% of the growth medium was exchanged three times per week. The HDMEA chamber was covered with a membrane permeable to oxygen (O_2) and carbon dioxide (CO_2) but not to water vapor, bacteria or fungi (Potter and DeMarse, 2001). Cultures were kept in a humidified, preservation incubator set at 37°C and 5% CO_2.

4.3. High density microelectrode array (HDMEA) preparation

A CMOS-based HDMEA was used for recording (Frey et al., 2010). The HDMEA has 11,011 electrodes arranged in a hexagonal pattern, with a pitch of 17 μm, yielding an electrode density of 3150/mm^2. Biocompatibility was obtained by an additional passivation of the CMOS device consisting of a stack of SiO_2 and Si_3N_4 layers, as described elsewhere (Frey et al., 2010). The culture chamber was fabricated from Epoxy resin (EPO-TEK 301-2) using a PDMS stamp to protect the culture area (2.5 mm x 2.5 mm). Before plating, HDMEAs were treated with oxygen plasma for 40 seconds at 20 W in order to render the surface hydrophilic and sterilize the HDMEA. The impedance of the Pt electrodes was decreased by electrochemical deposition of Pt black immediately after plasma treatment as described elsewhere, with minor modifications (Bakkum et al., 2013). The MEA surface was kept hydrophilic by filling it with sterile distilled

water. The day of the culture plating, MEAs were coated with Poly-D-Lysine (Sigma-Aldrich, P7280, concentration of 50 μg/ml in PBS) for one hour at room temperature, and washed four times with sterile distilled water afterwards. Prior to plating the cells, the electrode area was wetted with laminin (Sigma-Aldrich L2020, final concentration 20 μg/ml in PBS) for 20 minutes in the preservation incubator.

4.4. Experiment overview

Ten successful experiments were performed with ten cultures from four different platings (Table S2). The age of the used cultures ranged from 14 days *in-vitro* (DIV) to 58 DIV. Previous studies have shown that both the activity of the network (Chiappalone et al., 2006) and the shape of EAPs (Weir et al., 2015) are stable after 14 DIV. Experiments were performed at least one day after a medium exchange session. HDMEAs were placed into a custom stage-top incubator with temperature, humidity, and CO_2 control (TOKAI HIT, INU-OTOR-RE). The temperature was regulated to 36.6°C. An experiment consisted of HDMEA recordings followed by immunofluorescence staining and microscopy.

4.5. HDMEA recordings

After transferring the plated HDMEA devices from the preservation incubator to the custom experimental incubator, the cultures were allowed to rest for half an hour, after which the recording was started. The HDMEA can simultaneously record from 126 electrodes, which were arranged in block configurations (e.g., 6 columns by 12 rows) and used sequentially to cover the whole electrode area. Each configuration's recording time ranged from one to three minutes using custom-made software in LabView (National Instruments).

4.6. Immunostaining

After the recording session, the cultures were fixed for immunostaining (Table S2). Cultures were washed with ice-cold phosphate buffered saline, fixed for 15 minutes at room temperature, followed by two PBS washes. The fixative was a freshly-prepared solution of paraformaldehyde (Sigma-Aldrich), 4% w/v in phosphate-buffered saline (PBS). For Culture 1, 0.005% glutaraldehyde (WAKO Chemicals) was added. Immunostaining was performed as previously described (Bakkum et al., 2013) with minor modifications. Briefly, samples were permeabilized by incubation for 10 minutes with PBS containing 0.25% Triton-X (Sigma-Aldrich). After three washes for five minutes with PBS, samples were incubated with blocking medium for 30 minutes. Blocking medium consisted of 1% bovine serum albumin (BSA, Sigma-Aldrich, A4161) in PBS with 0.1% Tween-20 (Sigma-Aldrich, P1379). Primary antibodies were then added directly to the blocking solution, and the samples were left overnight at 4°C. The next day, the samples were washed three times for five minutes with PBS, and, thereafter, incubated for one hour with secondary antibodies followed by three PBS washes for five minutes. Nuclear staining was obtained by incubation for one minute with DAPI (300 nM in PBS), followed by three PBS

washes. Samples were stored at 4°C prior to imaging. Control experiments showed that the position of soma and axons were not affected by immunostaining (**Figure 4-1**).

The used primary antibodies included rabbit anti-β3-tubulin (ab18207, abcam) at 1:1000 dilution, and mouse anti-Neun (MAB377, Millipore) at 1:200 dilution. Secondary antibodies included Alexa Fluor 555 goat anti-rabbit (A-21429, Life technologies) at 1:200 dilution, and Alexa Fluor 488 goat anti-mouse (A-11029, Life technologies) at 1:200 dilution.

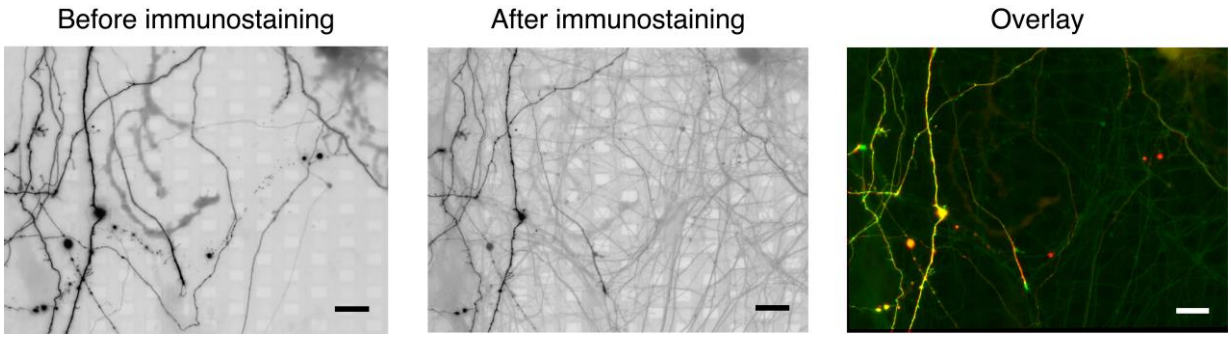

Figure 4-1.Fixation had minimum effects on neuron morphology and location.
Cells were lipofected with pCAG:EGFP at 6 DIV. One week later, live imaging was performed inside the stage-top incubator. The culture was then fixed and immunostained, and then the same area was imaged again. The right, composite, image is their registered overlay image. Registration was performed with ImageJ. Scalebars 20 μm.

4.7. Fluorescence microscopy and image processing

Fluorescence microscopy was performed with an Olympus BX61 epi-fluorescence microscope, equipped with a water-immersion objective (LUMPlan FL N,40x/0.8 W). Metamorph software was used for acquisition and assembly of the images. After calibration of the Metamorph-controlled stage, successive patches were acquired and then stitched together to produce one final image for each wavelength. Filters used were GFR, RFP, DAPI, and infrared (IR). IR imaging allowed for visualization of the electrode surface. The images obtained at different wavelengths were aligned via Metamorph or Matlab (Mathworks) algorithms.

Further image processing was performed with Matlab and FIJI. To improve the registration performance and identification of thin neurites, I processed the acquired fluorescence images in the following way. The gamma setting was modified to enhance weak intensity signals. The picture was then inverted, converted to 8-bit grayscale, the levels were adjusted for the whole picture, and the image was saved again in png format. This procedure increased the intensity of the weaker signals, allowing for clearer visualization of the background electrodes and weakly stained neurites. The resolution of the final image was 0.176 μm per pixel.

Matlab was used for registering the modified microscopy images to the recorded data. The electrode template was registered to the IR image by using the electrode edges at the corners of the array as control points at high magnification. Affine transformation was then used. All other

wavelengths were registered to the electrode template with the same transformation. This procedure resulted in good quality registration of the electrodes. Before continuing with further data analysis the electrode template and the microscopy images were overlaid and observed at high magnification. This allowed for evaluation of the registration quality of all experiments/figures, and no issues were detected.

4.8. Generation of activity maps indicating threshold-crossing events

Activity maps were generated the following way. After band-pass filtering (500 – 3000 Hz) of the electrode signals, events with a negative peak height larger than seven times the standard deviation of the background noise were identified. Detection thresholds of five to seven times the noise levels are commonly used (Stegenga et al., 2008; Srinivas et al., 2007; Baltz et al., 2010; Sun et al., 2010). For these presumptive spike events the firing rate was calculated for the whole recording interval (including burst and inter-burst intervals) and for all electrodes. The resulting whole-array firing rate map was color-coded as squares centered at the electrode coordinates on top of the immuno-fluorescence image (**Figure 4-2**). Using this procedure, active areas could be easily distinguished from silent ones. Electrodes recording threshold-crossing events were termed active electrodes. Electrodes which recorded activity at a rate less than 0.2 Hz were termed as silent electrodes.

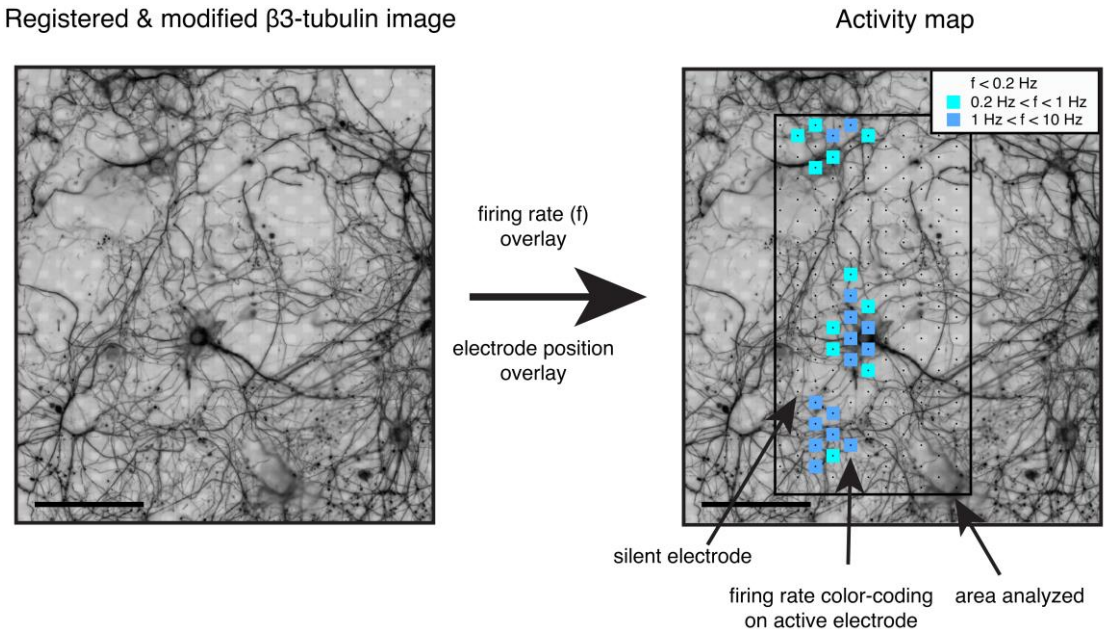

Figure 4-2. Generation of activity maps. The registered immunostaining images were used to distinguish between somatic and axonal sources of activity. The firing rate of each electrode was calculated with a threshold detection algorithm. The firing rate of each electrode was plotted on top of the β3-tubulin image, with the addition of color-coded squares on top of active electrodes. Electrodes which recorded activity at a rate less than 0.2 Hz were termed as silent electrodes. The inset shows the color code for the firing rate range, f, in Hz. Scalebars: 100 μm.

4.9. Somatic and axonal spike-triggered averaged footprints

The appearance of threshold-crossing events is one indication of putative neuronal activity. I performed my analysis based on spike-triggered averaged footprints which can more precisely indicate the electrodes recording neuronal signals. The procedure involved selecting three electrodes to perform spike-sorting with, getting the spike timings of the events from the spike sorted cluster, and finally getting the averaged traces for multiple neighboring electrodes.

Spike sorting was performed with UltraMegasort (UMS) (Hill et al., 2011). UMS is a freely available Matlab toolbox, which was adapted as necessary for use with HDMEA toolboxes and datasets. After a spike detection, the algorithm was blind to other threshold crossings for 0.8 ms. The EAPs were then aligned, and 2.5 ms of recordings (50 samples at 20 kHz) of each waveform were stored. Individual spikes were aligned with respect to the peaks of the largest spikes.

The first part of the spike sorting procedure was automatic and consisted of the following steps, already implemented by UMS: Principal component analysis was performed, followed by K-means clustering. The interface energy similarity metric was used to identify clusters very close to each other [Fee 1996b UMS]. If two clusters had high interface energy, they were clustered together, and the interface energies were re-calculated until the aggregation stop criterion was reached. The aggregation stop criterion value was set to 0.001. Briefly, higher values of this criterion allow for more aggregation.

The second part of the spike sorting procedure involved the supervised evaluation of clustering. The principal component analysis (PCA) space and refractory period violation (RPV) were taken in account so that single, well-isolated clusters with minimum RPV were used. An example of a spike sorting procedure to separate neuronal clusters is shown in **Figure 4-3** . The automatic spike sorting by UMS, together with the supervised evaluation procedure, were effective in separating clusters of large somatic spikes from the small ‘contaminating’ neuritic spikes (**Figure 4-4**), as well as for the large axonal spikes.

The timing of the spike-sorted activity was used to extract signals from multiple neighboring electrodes. A spatial somatic or axonal footprint was generated, depicting the spike-triggered average (STA) signal for each electrode footprint. For this and subsequent analysis the raw traces were used, after oversampling at 320 kHz. Such oversampling improves the relation to the analog signal, especially at the spike peak and valley (Blanche and Swindale, 2006).

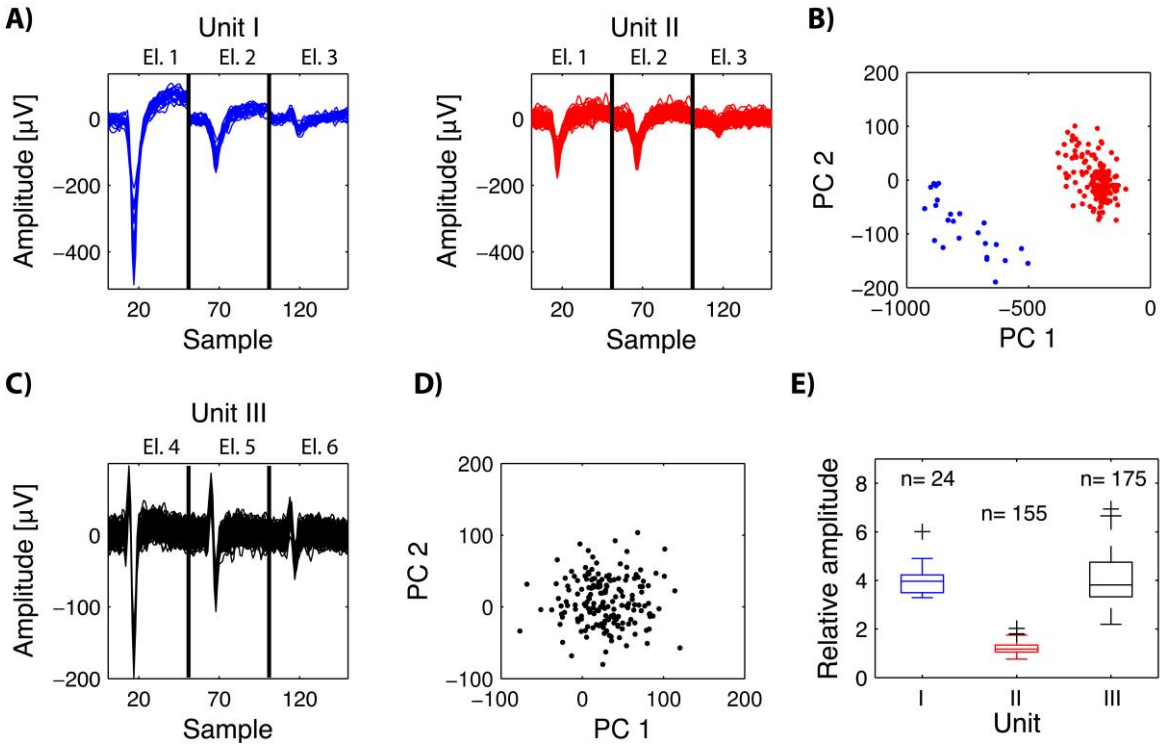

Figure 4-3. **Illustration of supervised spike sorting with UltraMegaSort using information from three electrodes(A)** Signals from three electrodes were classified into two well-separated units, unit I (blue) and unit II (red). The samples from the three electrodes were concatenated to give one large vector. **(B)** PCA space for the first two principal components for units I and II. **(C)** Another set of electrodes recorded single-unit activity, unit III. **(D)** PCA plot for the unit in **(C)**. **(E)** Box plot showing the relative amplitude value for each of the three units. For each detected spike, the ratio of the negative peak value of the first and second electrode was used. The color of each group corresponds to the color of the corresponding unit (red, blue or black). Boxplot lines represent the median, the edges are the 25th and 75th percentiles. The whiskers extend to the most extreme points not assigned as outliers. Outliers are shown independently with cross-marks.

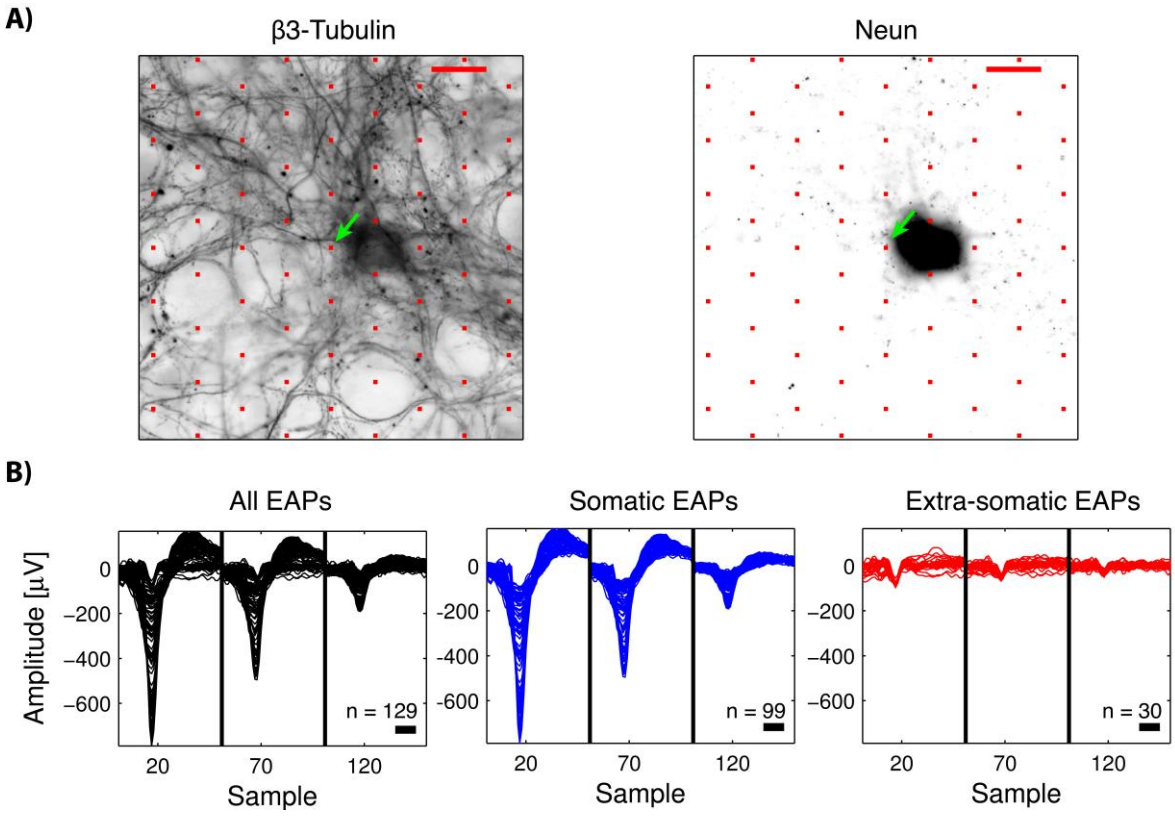

Figure 4-4. Electrodes close to a single neuron might record activity from more than one source.(A) An electrode close to a single neuron was selected indicated by the green arrow. β3-tubulin and Neun staining showed one nearby neuronal soma from a multipolar neuron. A complex network of neurites is visible in its periphery. The red squares represent the center of the electrodes. Global gamma, brightness and contrast modifications were performed. Scalebars 20 µm. **(B)** EAPs of all identified spikes from the selected electrode (left black traces), and after the spike sorting procedure which resulted in the separation of somatic (middle blue traces) and non-somatic spikes (right red traces). Scalebars 0.5 ms.

4.10. Spike shape feature analysis of representative somatic and axonal electrodes

From each somatic and axonal footprint the electrode with the highest STA amplitude was selected as representative for further analysis. I only used one electrode per footprint to avoid duplicate data and any resulting bias. For each representative electrode two types of analysis were performed.

A first analysis involved spike shape features of the STA waveshape. Three spike shape features were used, the amplitude, half-width and trough-peak width. The amplitude of an STA was defined as the amplitude of the main negative peak. The half-width was defined as the duration of the STA main phase with values below 50% of the negative peak. The trough-peak width was defined as the time from the main negative peak to the first positive peak (Weir et al., 2015; Robbins et al., 2013; Becchetti et al., 2012). These features are shown in **Figure 4-5**. The relative standard deviation (rstd) was calculated as the standard deviation of the normalized traces to the peak-to-peak amplitude of the average trace (Jäckel et al., 2012). Classification of STAs into different spike types was performed with a cross-correlation based algorithm. The cross-correlation of the STAs to pre-extracted EAP samples of the four types was calculated. STAs and pre-extracted samples were amplitude-normalized. Each STA was assigned to the type with which it had the highest cross-correlation value.

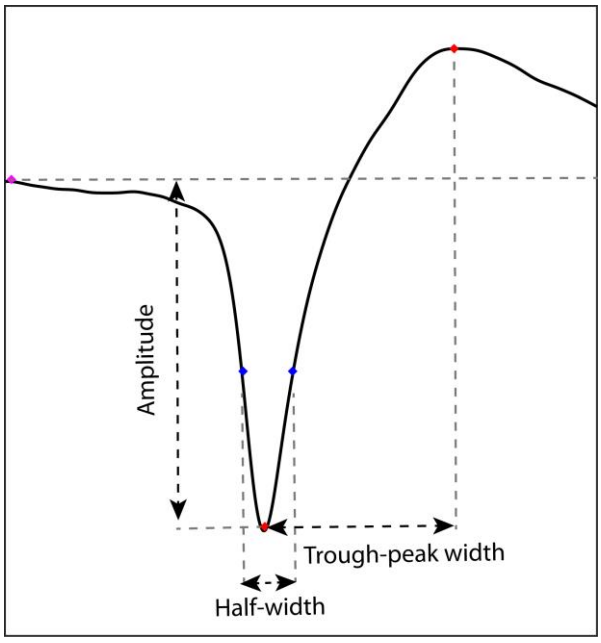

Figure 4-5. Illustration of spike shape measures used for comparison of somatic and axonal spikes. The amplitude was defined as the amplitude of the main negative peak. The half-width was defined as the duration of the main phase with values below 50% of the negative peak. The trough-peak width was defined as the time from the main negative peak to the first positive peak. Shown here is a spike sample and the corresponding points found by the algorithms used: zero-point (magenta dot), trough-peak width (red dots), half-width (blue dots).

The second type of analysis utilized the same features, but at individual-spike resolution (rather than the STA). The continuous firing rate (cFR) was calculated for each spike according to the following equation:

$$cFR(t) = d * r(t - \Delta t) + (1 - d) * \frac{1}{\Delta t}$$

where Δt is the time between current and previous spike, and *d* is the exponential decay term ($d = e^{-\Delta t/\tau}$), with τ = 100 ms (Stratton et al., 2012). While the inter-spike interval (ISI) represents the instantaneous firing rate, the cFR rises slowly during the burst, with a low cFR at the beginning of the burst (**Figure 4-6**). An exponential function was fitted to the spike shape features versus the cFR by minimizing the sum of squared residuals,

$$g(x) = y_0 * e^{bx} + y_\infty$$

This procedure resulted in a good fit for both somatic and axonal data and provided an adaptation profile for each unit. The adaptation was calculated as

$$AR = \frac{y_\infty}{y_\infty + y_0} - 1$$

and expressed in percent. The two-tailed Mann-Whitney test was used to test for differences between somatic and axonal distributions.

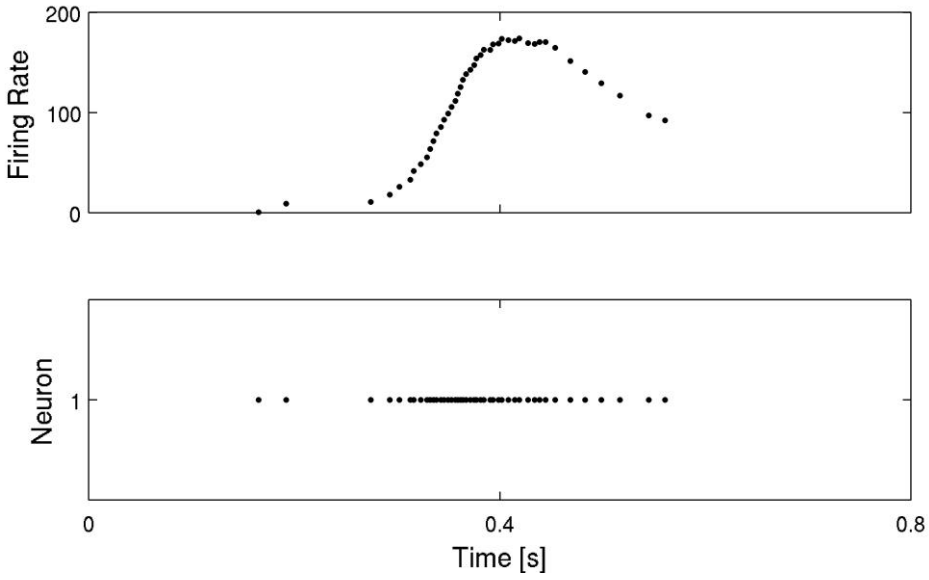

Figure 4-6. Minimum firing rate occurs at the beginning of a burst, while maximum occurs midway. The top axis shows the development of the continuous firing rate (cFR), calculated for each spike. The bottom plot shows the spike timings of the same neuron.

5. Results

5.1. Characterization of low-density cultures on an HDMEA

First, the morphology of low-density cultures on the HDMEA was investigated. Cultures were stained with β3-tubulin to visualize axons and dendrites, Neun for neuronal nuclei, and DAPI for nuclei of all cells. **Figure 5-1** shows a representative culture at 29 DIV on the HDMEA with 10,000 plated cells. β3-Tubulin staining was prominent all over the array, but denser staining was seen in the areas surrounding the electrode array (outside the gray box in **Figure 5-1A**). This suggests that neurites could probably attach and grow better on the area surrounding the array, rather than on the rough electrode surface, which was also coated with Pt black. Neun staining showed that there were single, isolated neurons, and aggregates on various parts of the electrode array. Finally, DAPI staining indicated that the majority of cells were non-neuronal.

Single neurons could be easily identified by the β3-tubulin staining, especially at a young age, when the complex structure of neurites is not so dense to obscure soma visualization. A zoom-in to a single neuron on top of the HDMEA can be seen in **Figure 5-1B**. The neuron has a pyramidal-like shape and basal dendrites radiating from it. Another neurite can be seen growing upwards, thicker and longer than the rest (white arrow), similar to the long apical dendrite in pyramidal neurons (Spruston, 2008). From the upper left side of the soma, there is an emanating long, thin neurite, which seems to be the axon (white arrowhead).

The surface of the HDMEA was not uniformly covered with neurons. Instead, some areas were covered only by neurites. A putative single axon is shown next to the neuron in **Figure 5-1B** (dashed white arrow) while neurite aggregates are shown in the bottom row of **Figure 5-1B**. The latter seemed to be axons, dendrites or a mixture of both, as β3-tubulin stains both dendrites and axons, while the large number of neurites prevents analysis of individual neurites.

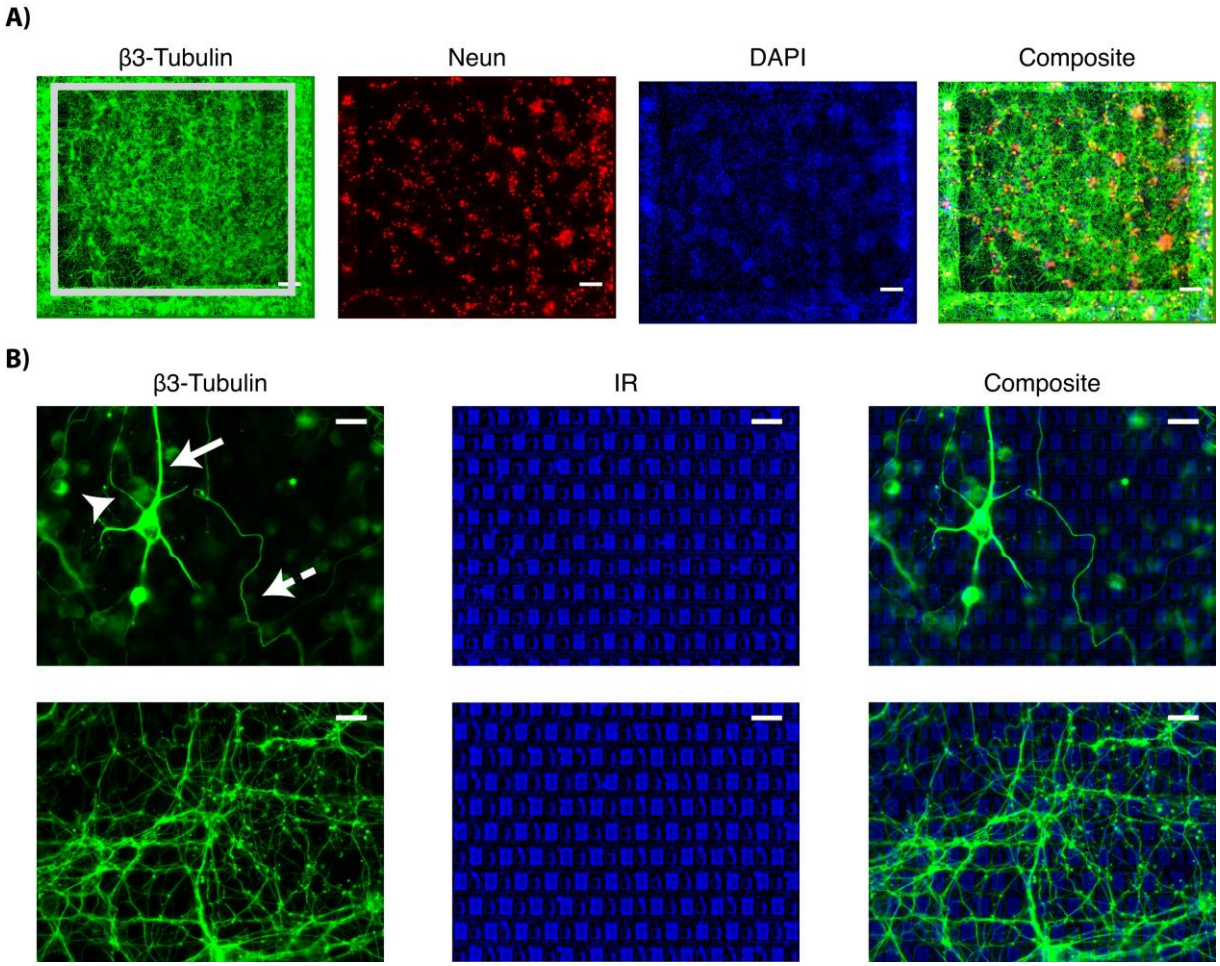

Figure 5-1. Morphology of low-density dissociated cultures on the HDMEA and identification of neurons and neurites on top of the electrodes. **(A)** A 10,000-cell culture is shown, fixed at 29 DIV. β3-tubulin, Neun and DAPI are shown, as well as the composite image. The gray rectangle in β3-tubulin image denotes the borders of the electrode area. Scalebars 200 µm. **(B)** Two examples of a field of view containing either one neuron (top row) or multiple neurites (bottom row). β3-tubulin stained axons and dendrites, while infrared (IR) imaging revealed the underlying electrodes. On the top image putative axons (arrowhead, dashed arrow), and a thick neurite (arrow) can be seen. Scalebars 20 µm.

5.2. Both neuronal somata and axons contribute to threshold-crossing events on MEAs

First, I tested the hypothesis that HDMEA electrodes can record neuronal electrical activity even in the absence of a near-by soma. Activity maps were generated, as described in the methods section, and these were observed in order to confirm or reject my original hypothesis. I noticed putative neuronal activity, defined as threshold-crossing events, in areas on top of, near-by, or far away from neuronal somata as will be further explained. This suggests that the HDMEA electrodes can record both somatic and axonal activity.

Figure 5-2A shows active electrodes below a neuronal soma (white arrow), as well as silent electrodes below a second neuronal soma (white arrowhead). Two electrodes near these neurons also recorded putative spike events (dashed white arrows). In addition, I typically observed threshold crossing events in areas far away from neuronal somata. **Figure 5-2B** illustrates that presumptive neuronal activity was recorded in an area with high neuritic density. A soma can be seen in the upper left side (white arrow). Although no somata can be seen at the center of the area, most of the electrodes recorded threshold-crossing events. Another example is shown in **Figure 5-2C**. Putative activity from a local, distal part of an axon (small white arrow) can be seen. The origin of this activity could be the highlighted axon (magenta arrows). Another interesting scenario is spiking activity that seems to be reaching the end of an axonal bundle (small green arrow). Overall, groups of active electrodes were found close to somata and neurites, with the group size ranging from one to tenths.

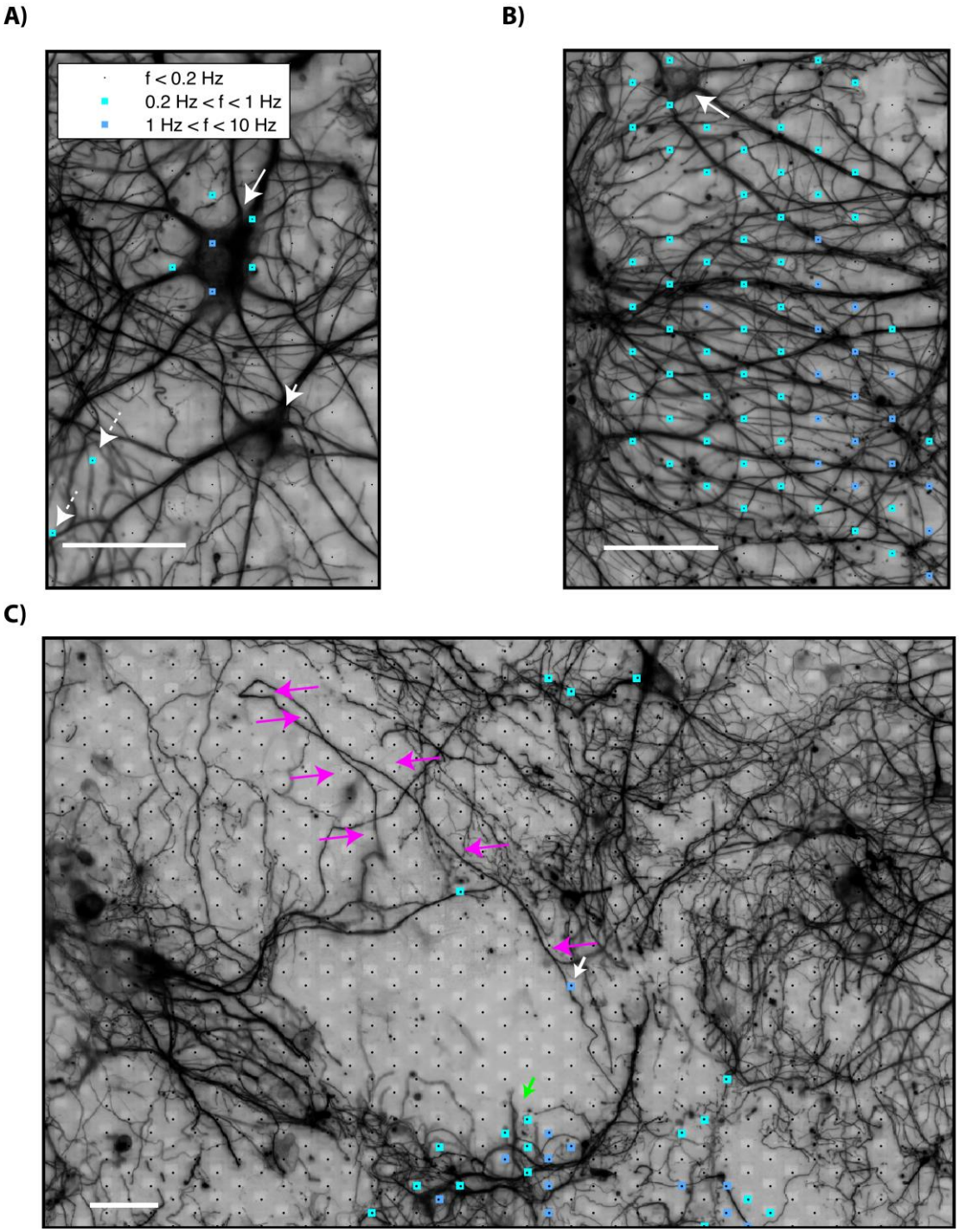

Figure 5-2. Identification of somatic and neuritic sources of presumptive spiking activity in HDMEA recordings. (A) Activity map of an area with two neuronal somata. One of them (white arrow) is active, while the other silent (white arrowhead). Near the two somata two more electrodes have recorded threshold-crossing signals (dashed white arrows). **(B)** An area of high neuritic density showed presumptive spiking activity. Only a soma at the upper left corner can be seen (white arrow). **(C)** A larger field of view of the electrode array with a low-density culture on top. Many active electrodes can be seen in areas distal to neuronal somata. Activity from the distal part of a highlighted axon (small white arrow shows the active segment, magenta arrows highlight the axon), and what seems to be the end of an axonal bundle (small green arrow) can be distinguished. Scalebars 50 µm. Color-coding scheme is the same for all pictures and depicted as legend in **(A)**.

In order to verify that the threshold-crossing events shown in the activity maps truly represent somatic or axonal activity I focused on the small surrounding areas containing the active electrodes, and belonging to the same electrode configuration. Spike sorting using three electrodes close to the active soma or axon produced the spike timing of the given soma/axon. Averaging over many neighboring electrode signals (raw, oversampled traces, 40-80 electrodes) generated the corresponding footprints, depicting the STA with respect to the activity of the given soma/axon. **Figure 5-3A** shows such a somatic footprint, while **Figure 5-3B** shows an axonal footprint. Both footprint areas were previously deemed as active (**Figure 5-2A**, and **Figure 5-2C**). The negative peak of the somatic electrodes could reach up to 300 μV, while that of the axonal electrodes up to 100 μV. STAs of three selected electrodes are also shown (large blue, red, magenta electrodes in the β3-tubulin images). The axonal spike shapes were tri-/bi- phasic and narrower than the somatic ones. Two more sets of axonal STAs with varying waveshapes are shown in **Figure 5-3C**, while their complete footprints are shown in **Figure 5-4**.

A nearby soma can be seen in the axonal footprint in **Figure 5-3B** (small white arrow). I sought to exclude this soma as the source of the recorded activity. Observation of the activity map (**Figure 5-2C**) showed absence of threshold-crossing events around this soma. Most importantly, the axonal STA footprint shows that there is no correlated activity between the active axon segment (white arrow in **Figure 5-3B**) and the nearby soma. Therefore, I believe it is safe to conclude that the origin of this signal is the distal part of the visualized axon. However, I cannot exclude other sources either.

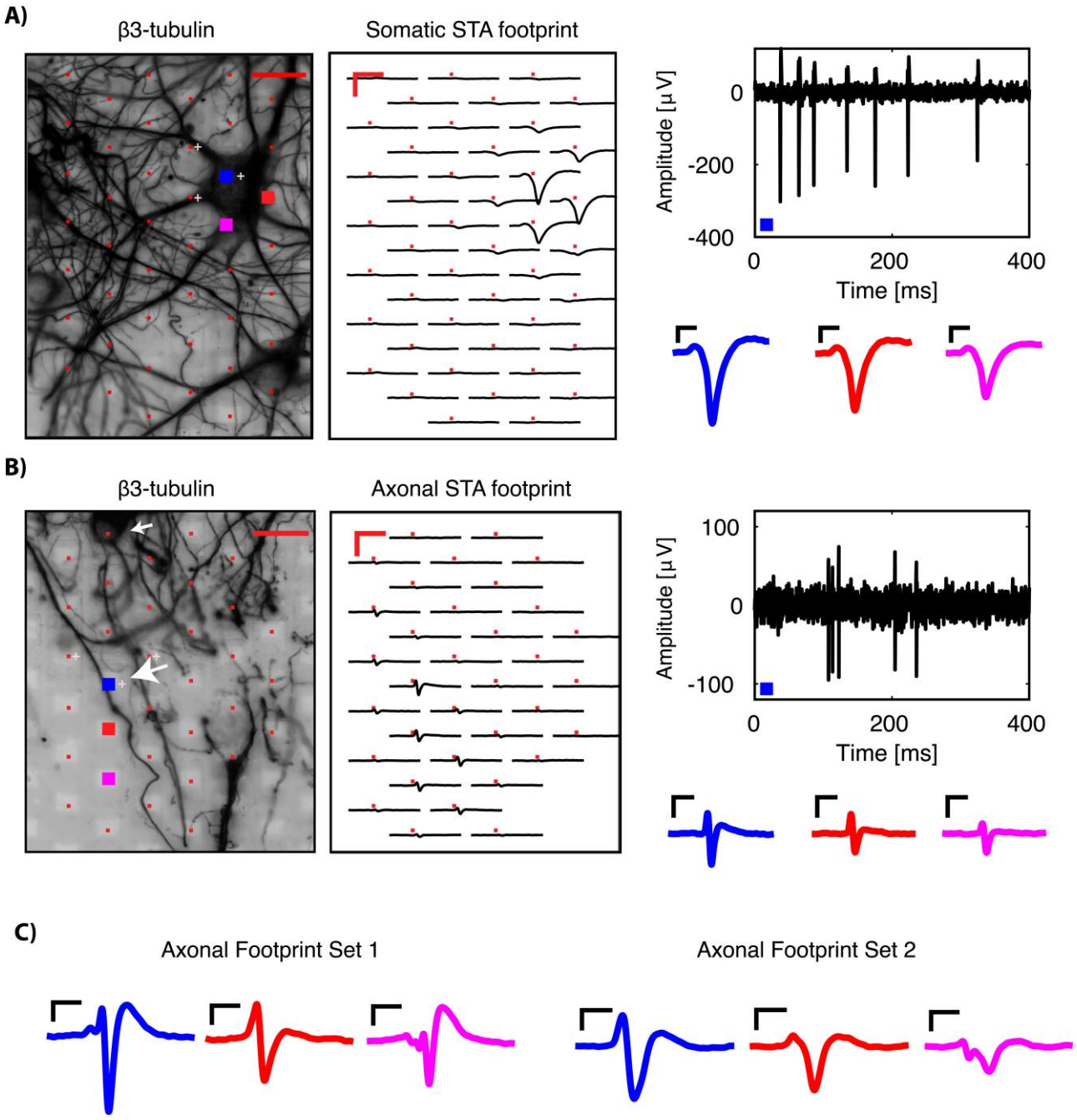

Figure 5-3. Examples of somatic and presumptive axonal footprints. Spike sorting and subsequent spike-triggered averaging resulted in a spatial footprint, depicting the STAs over many neighboring electrodes in the same recording block. **(A)** Examination of the signals from the neuron shown in **Figure 5-2A**. Three electrodes were used to perform spike sorting (white crosses, next to the red electrodes in β3-tubulin image). The somatic footprint shows the STAs for the near-by electrodes, aligned on the timing of the spike-sorted activity. A band-pass-filtered (100 – 5000 Hz) signal from the large blue electrode is shown on the right, where the negative peak can reach up to 300 μV**.** Three STA examples are also shown for the three large (blue, red, magenta) electrodes in β3-tubulin image. **(B)** Similar to **(A)**, for the axonal footprint (white arrow in **Figure 5-2C**). **(C)** Two more sets of STA examples from presumptive axonal footprints. The complete footprints are shown in **Figure 5-4**. Scalebars 20 μm for β3-tubulin staining, 2 ms/200 μV for the footprints, 0.5 ms/50 μV for the STA examples

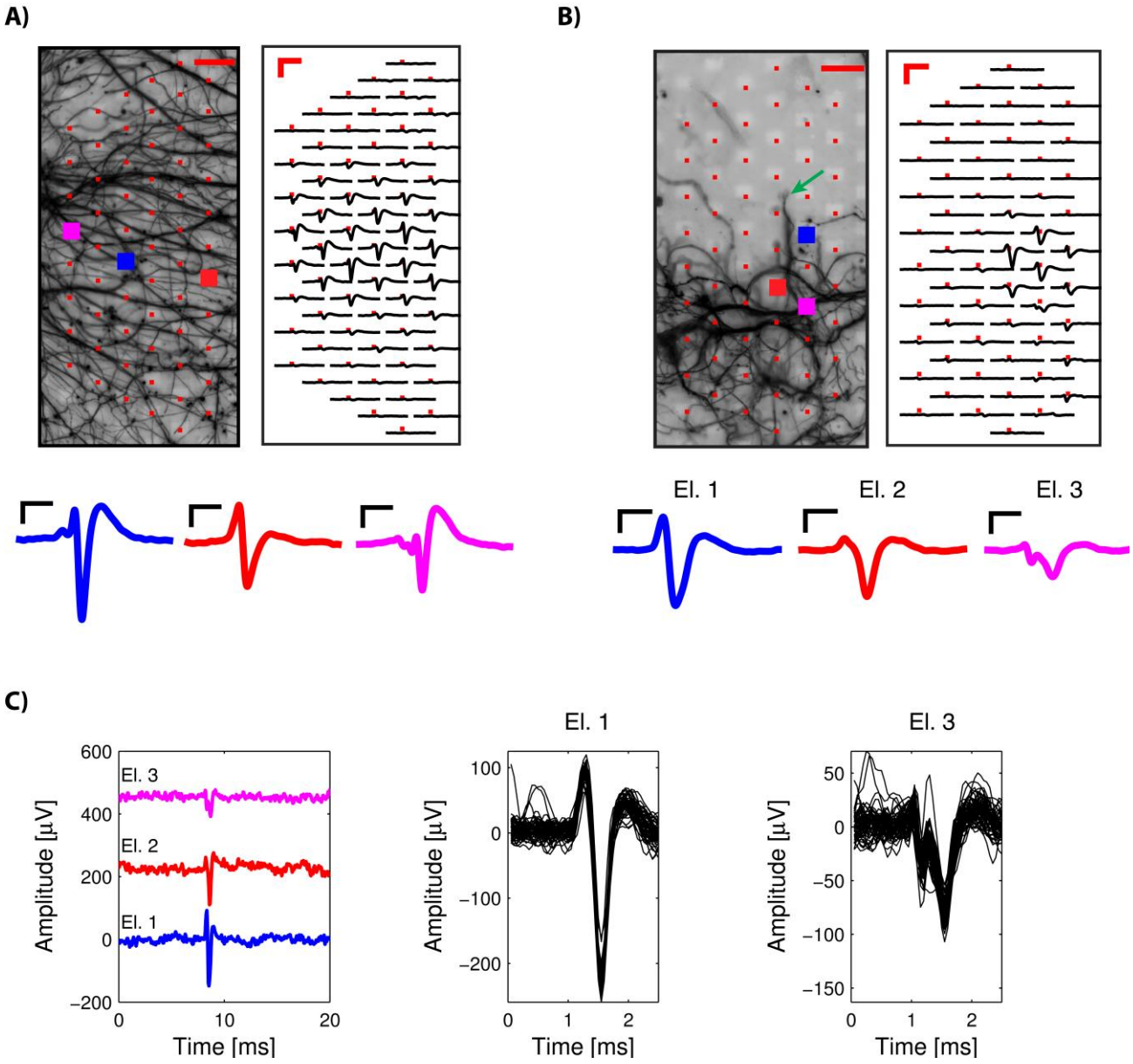

Figure 5-4. Two more examples of axonal footprints whose STA examples are shown in Figure 5-3. (A) A region of high neuritic density exhibiting putative spiking activity. The footprint shows the STA for the near-by electrodes, aligned on the timing of the spike-sorted activity. Three STA examples are shown for the three large (blue, red, magenta) electrodes in β3-tubulin image. **(B)** An axonal footprint showing what seems to be spiking activity reaching the end of axonal bundle (see **Figure 5-2**). In the β3-tubulin image some filopodia-like structures can be distinguished (green arrow). The three electrodes highlighted (large blue, red, magenta electrodes in β3-tubulin image) exhibited different STA shapes. **(C)** Further analysis of the STAs in the three electrodes shown in **(B)** indicated that they do not fire in isolation. Electrode 3 recorded STAs with two negative peaks, but the two negative peaks were never recorded in isolation. All the spikes identified had a similar shape.

5.3. Comparison of somatic and presumptive axonal spike shape features

Lastly, I performed a comparison of somatic and axonal spikes. I identified 26 somatic and 29 presumptive axonal footprints. In these footprints I performed spike sorting in an identical way to the previously-analyzed footprints. The resulting clusters had consistent waveshapes and very low RPV levels (Table S3). From each somatic or axonal footprint the electrode with the highest amplitude was selected as representative of the particular footprint. One electrode per footprint was selected to avoid using data from the same source twice. I compared the three spike shape features among somatic and axonal STAs, as well as their activity dependency.

In my data, I could not precisely measure the distance of the active axonal segment to its respective soma. Instead, I calculated the distance of the representative electrode to the nearest soma by extracting a region of 200 x 200 μm^2, centered on the representative electrode, from the immunofluorescence images. After identification of near-by neurons, a line was drawn from the electrode to the center of the nearest neuron on the β3-tubulin image. 23 out of the 29 representative axonal electrodes were at least 100 μm away from the nearest soma, while 6 were between 50 and 100 μm away from the nearest soma. However, as **Figure 5-3B** illustrates this measure underestimates the true distance of the active axonal segment to its respective soma. The same procedure was repeated for somatic footprints. In this case, the distance to a second soma was calculated. 15 out of the 26 representative somatic electrodes were between 50 and 100 μm away from a second neuronal soma, 6 were at least 100 μm away, while 5 were between 15 and 50 μm away.

Firstly, I compared the spike shape features of the representative electrodes' STAs. The distributions of the somatic and axonal amplitude, half-width and trough peak width were significantly different from each other (Mann-Whitney test, $p< 0.001$ for all three cases). **Figure 5-5A-B** shows the distribution of the three features for each STA. Somatic STA amplitude, half-width, and trough-peak width distributions were not completely separated from the axonal ones, but instead had overlapping values. The median of the amplitude in all somatic STAs was -171.59 μV whereas for the axonal STAs was -73 μV. Thus, although the large axonal spikes are large in the sense that they can be recorded and identified by a threshold-detector they have almost half of the amplitude of the somatic spikes. The median of the half-width in all somatic and axonal STAs was 250 μs and 130 μs respectively. The median of the trough-peak-width across the somatic and axonal STAs was 700 μs and 380 μs respectively.

I then used a template-matching algorithm to assign each representative somatic or axonal STA to one of four putative types (notice the four EAP types shown at the center of **Figure 5-5**). Type 1 had a broad monophasic shape, Type 2 had a broad biphasic shape with a positive peak after the main negative peak, Type 3 was triphasic with the larger positive peak before the main negative peak. Finally, Type 4 had a narrow, symmetric triphasic shape, similar to the one reported *in-vivo* by Robbins et al. (Robbins et al., 2013). Each somatic or axonal STA was assigned to the type with the highest cross-correlation value. 24 out of the 26 somatic STAs were classified as Type 1 or 2. 22 out of the 29 axonal STAs were classified as Type 3 or 4 (**Figure 5-5C**). This provided further evidence that the somatic and axonal spikes we analyzed belong to distinct groups. Finally, the RSTD distribution of axonal spikes was in the range of 0-0.3, approximately half of the maximum value of somatic STAs ($p = 0.0068$, **Figure 5-5D**).

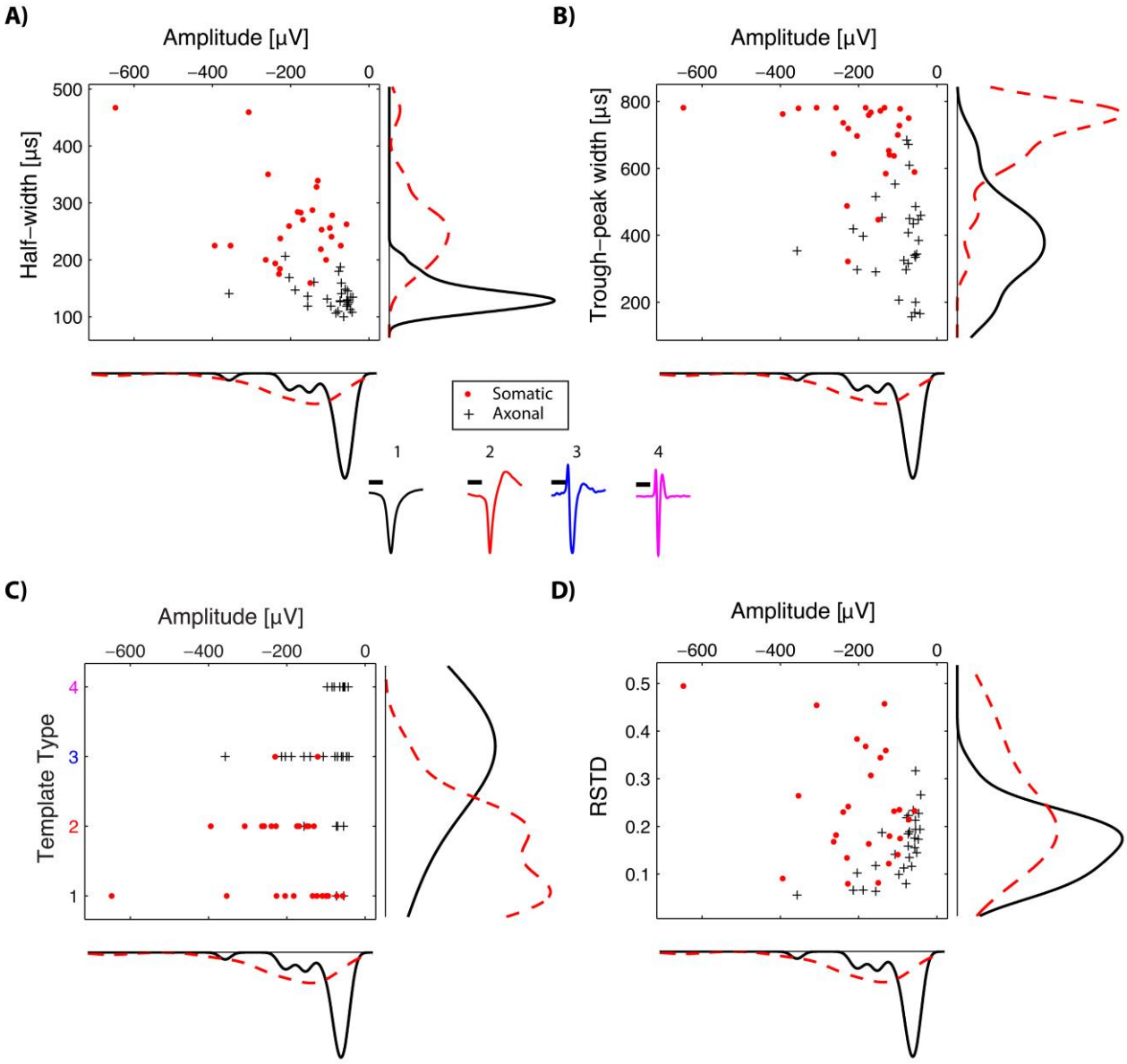

Figure 5-5. Comparison of somatic and presumptive axonal spike properties. (A) Scatter histogram for the amplitude and half-width for the representative somatic (n =26) and axonal (n = 29) representative STAs. On the sides kernel density plots are shown. **(B)** Similar to **(A)**, but for the amplitude and trough-peak width. **(C)** A template-matching procedure was used, and the spike shapes for axonal and somatic STAs were classified accordingly. There is a clear distinction between the somatic and axonal classification results. **(D)** Scatter histogram for the RSTD values and amplitude. Somatic STAs have wide distribution, while the axonal STAs RSTD is narrower. At the center the four types used during template classification are plotted with different colors. Each color represents a different template type, as in **(C)**.

The median value of 380 μs for the axonal spikes' trough-peak width seemed to be large, especially considering that the axonal spikes found by Robbins et al. had an average trough-peak duration of less than 180 μs (Robbins et al., 2013). However, the study by Robbins et al. focused only on spikes with a narrow triphasic shape, while the average found in this study included three different types. Analysis of the axonal STAs which were assigned to the triphasic template Type 4 indicated that they had a median amplitude of -61 μV, a median half-width of 114 μs, and a median trough-peak width of 200 μs. On the other hand, the axonal STAs which were assigned to the template Type 3 had a median amplitude of -92 μV, median half-width of 143 μs and median trough-peak width of 426 μs. This suggests that not all of the axonal spikes we recorded had narrow triphasic shape.

I then investigated the dependence of the spike shape features to the firing frequency by using the cFR information and analyzing the activity of representative electrodes at a single-spike resolution. I fitted an exponential function to the cFR data. Somatic spikes mostly showed a steep adaptation profile, while axonal spikes showed shallow profiles (**Figure 5-6A**). Adaptation of somatic spikes could reach up to 70 %, while axonal spike adaptation exhibited much smaller magnitude. A similar situation occurred for the half-width, while the trough-peak width did not show significant differences (**Figure 5-6B**).

The previous analysis based on the immunofluorescence data might have suffered from human bias or other immunofluorescence-related issues. Therefore, I decided to perform a blind analysis based on the template matching approach, which does not suffer from related issues. We used data from ten cultures/recordings, performed spike detection at each electrode (threshold set at seven times the noise), aligned the spike peaks, and extracted the average spike. Only electrodes recording an average spike having negative peak amplitude of at least 100 μV, with an RSTD lower than 1, and more than 100 spikes were used. Each average spike was assigned to a template type and an exponential curve was fitted to the features, as previously described.

The above conditions resulted in a total of 6463 average spikes from an equivalent number of electrodes. Results indicated that axonal (Type 3 and Type 4) spikes are narrower than somatic (Type 1 and Type 2), and they represent less than 15% of the spike population (**Figure 5-7A-B**). Axonal spikes exhibited less adaptation than somatic spikes (**Figure 5-7C**).

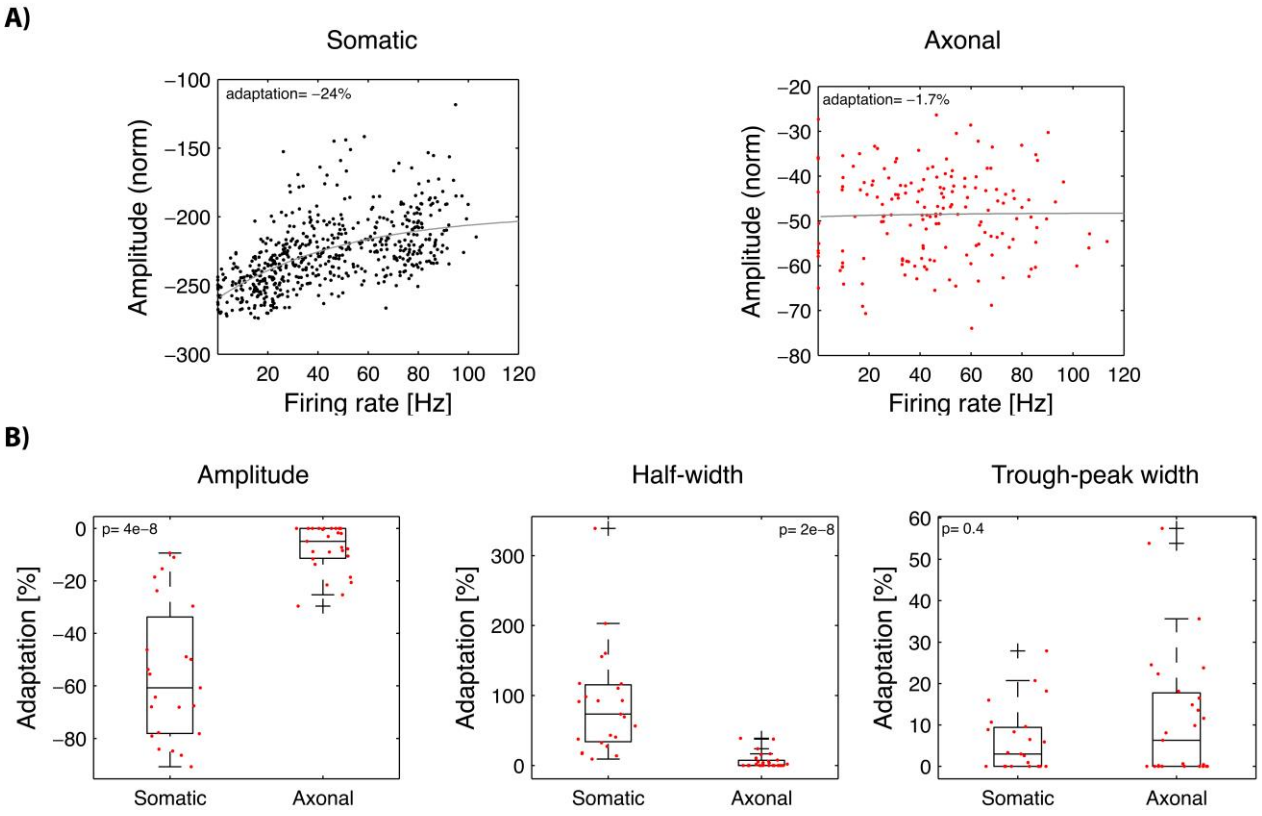

Figure 5-6. Adaptation properties of somatic and presumptive axonal spikes. (A). The continuous firing rate (cFR) was calculated for each spike and an exponential line was fitted to the spike shape features. Somatic spikes (top row) displayed steep adaptation profiles. Axonal spikes (bottom row) displayed mild adaptation profiles resulting in small negative or positive adaptation values. **(B)** Comparison of the adaptation values of the somatic and axonal units. Red dots represent the population for each boxplot. A small jitter in their x-values was introduced to assist in visualization. Boxplot lines represent the median, the edges are the 25th and 75th percentiles. The whiskers extend to the most extreme points not assigned as outliers. Outliers are shown independently with cross-marks.

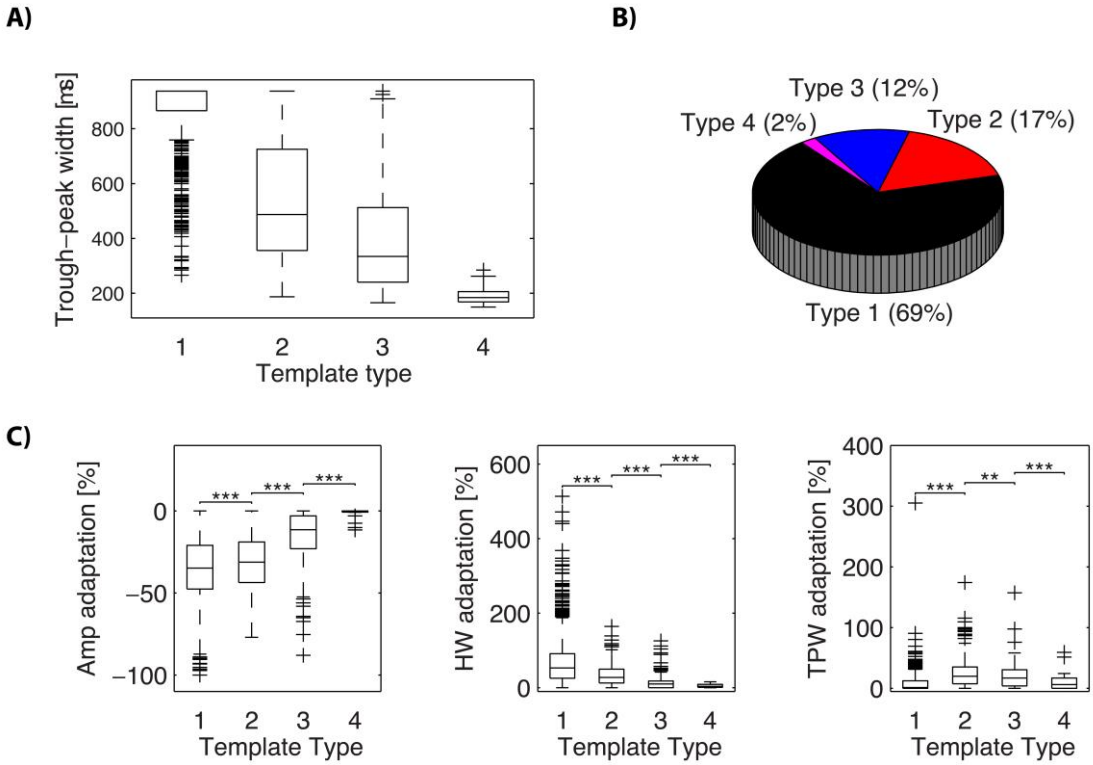

Figure 5-7. Adaptation profiles of different spike types, as identified by a template-matching algorithm. (A) The population assigned to each template type had different trough-peak width distributions. Wide spikes were assigned as template Type 1 and Type 2, while narrow spikes were assigned as Type 3 and Type 4. **(B)** Type 3 and Type 4 spikes represent a small percentage of the population of spikes recorded by the HDMEA (data from n = 6463 electrodes, ten cultures). **(C)** Spikes assigned to template Type 3 and Type 4 exhibit less amplitude and half-width adaptation than Type 1 and Type 2. Templates can be seen at the center of **Figure 5-5**. Amp: amplitude, HW: half-width, TPW: trough-peak width. Significance levels: **: 0.01; ***: 0.001

5.4. Tracing the axonal arbors of single neurons

The HDMEA system has the capability to switch electrode configurations in a matter of milliseconds. This allows specialized experiments where the electrodes are selected each time according to the needs of the experiment. One useful type of experiments arises by selecting a fixed somatic electrode to record from, in all configurations, while successively scanning the whole array until all electrodes are recorded from. This results in the spike timing of the soma, and the signals from all electrodes could then be averaged to produce the full neuronal footprint. This is an alternative technique for axonal electrophysiology with the benefit that the full arbor can be electrically visualized.

Such an experiment is shown in **Figure 5-8**. First, the spike timing of the soma was extracted by detecting the spikes from the selected electrode. Signals from all electrodes were then averaged and plotted. **Figure 5-8A** illustrates the distinct phases of an AP. First (t=0 ms), the negative peak is localized and can be sensed in a small area. At 0.2 ms later, negative signals can be recorded from more electrodes, around this area. At t = 1.25 ms the spike has moved to the axonal arbors and distinct pathways can be seen. As can be seen, the axonal signals are of very small amplitude, about -5 μV. This value was indeed a good threshold value to separate the noise from the signal (**Figure 5-8B**). Plotting the negative peak and delay of all signals above this threshold allowed me to trace the axonal arbor of the neuron. The temporal information is lost, but the spatial extend of the arbors and the corresponding signals can be visualized (**Figure 5-8C**). In this experiment, the axonal conduction velocity was also calculated at 0.39 m/s. This value is close to velocity values of unmyelinated axons (Debanne, 2004).

I then investigated the distance-amplitude relationship for the somatic signal. While **Figure 5-8C** shows how spike amplitude is decreasing as the spike propagates to the axonal arbor, **Figure 5-8D** shows the dependency of the amplitude to the distance of the recording electrode. The amplitude was seen to decrease with distance, reaching noise levels at about 100 μm from its origin. However, the return current (small positive signals, arrow in **Figure 5-8D)** can be obviously seen.

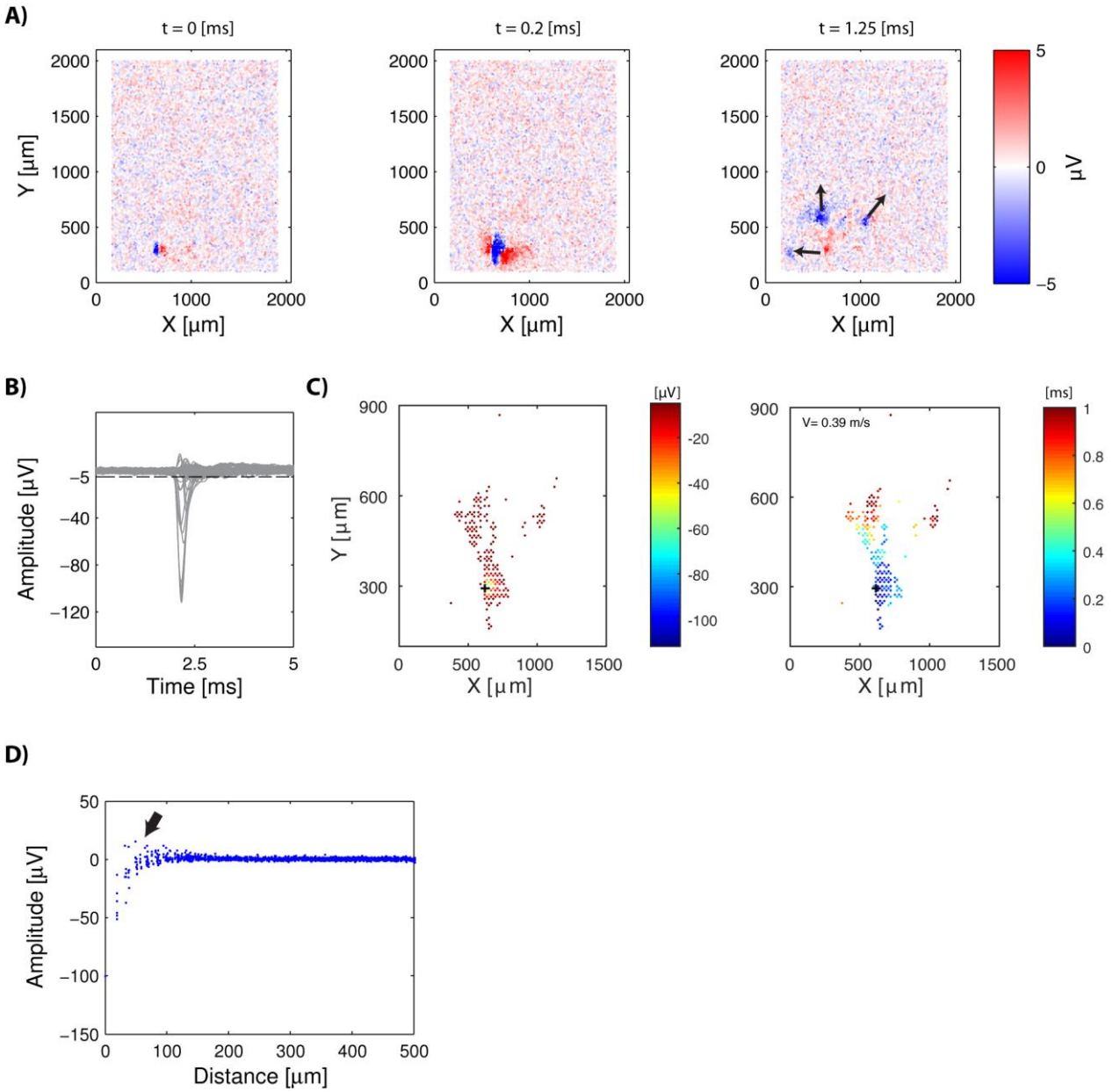

Figure 5-8. Tracing the full axonal arbor of single neurons.(A) Footprint of full neuronal arbor during an action potential. The spike initiates at t=0 and then propagates through distinct axonal arbors (arrows at t= 1.25 ms). **(B)** A threshold of 5 µV was deemed appropriate to separate small axonal signals from noise. The plot shows signals of 1000 electrodes, and the corresponding threshold. **(C)** Plotting of the negative peak value of all electrodes with signals which crossed the threshold revealed the axonal arbor of the respective neuron. **(D)** Distance-amplitude relationship of action potentials. Arrow indicates positive signals, arising from the return current.

6. Discussion

6.1. Origin of large-amplitude axonal spikes in MEA recordings

I plated low-density dissociated cultures on a HDMEA. I assigned electrodes as close to sub-neuronal somatic or neuritic segments, for further electrophysiological analysis by using information from immunostaining. My study was a first attempt to demonstrate the ability of recording large amplitude signals from both somatic and axonal segments in open-well cultures on HDMEAs.

Very low spiking contamination is expected in my recordings, in agreement with other studies using sparse neuronal cultures (Ullo et al., 2014). One of the characteristics of such cultures is the relatively high level of silent cells, as was observed in my data, rather than multi-unit activity. The majority of somatic (78%) and axonal clusters (95%) were the only clusters found in the recorded data. The rest included clusters of small neuritic spikes (see **Figure 4-4**). In the utilized clusters the average RPV was minimum (0% and 0.4% for somatic and axonal footprints with 1.5 ms refractory period parameter).

I identified axonal spikes up to an amplitude of 400 μV. The distance of the analyzed representative axonal electrodes to the nearest soma was larger than 50 μm. In the majority of cases analyzed here the distance was also larger than 100 μm. Since the axon initial segment, the site of AP initiation, is usually considered to be up to 75 um from the soma (Kole et al., 2008; Grubb and Burrone, 2010; Meeks et al., 2005; Meeks and Mennerick, 2007) it is highly probable that these spikes are not axon initial segment spikes. Although my data do not reveal exactly the distance of the active axonal sites to their respective somata, the axonal example seen in **Figure 5-3B** seems to be a very distal part of an axon, if the origin of the signal is indeed the long, highlighted axon. It is also peculiar why this specific part of the axon showed high-amplitude activity.

Axonal signals have been previously recorded and analyzed with tetrodes (Robbins et al., 2013), patch pipettes (Meeks et al., 2005), passive MEAs (Dworak and Wheeler, 2009), and HDMEAs (Bakkum et al., 2013; Lewandowska et al., 2015). Axonal signals originating from the thin axons are generally of lower-amplitude than somatic signals, which can negatively affect their detection (Khodagholy et al., 2014; Bakkum et al., 2013). To overcome this limitation, 'signal-amplification' polydimethylsiloxane (PDMS) microtunnels were implemented, which resulted in the recording of large amplitude, up to 200 μV, axonal EAPs on a passive MEA (Dworak and Wheeler, 2009). Similar structures on a HDMEA (Lewandowska et al., 2015) resulted in axonal spikes as large as 2 mV. The 'amplification' of axonal signals in microtunnels stems from an increased extracellular resistance, which in turn is imposed by the reduced volume of the extracellular fluid restricted by the microtunnels (Fitzgerald et al., 2008).

Axonal spike propagation has been also recorded from retina slices where the axons are at the bottom side of the tissue, in contact with the MEA surface (Fiscella et al., 2012; Zeck et al., 2011). In Fiscella et al. a membrane was lightly pressed against the tissue, and with this protocol

both somatic and axonal spikes were identified. Slight mechanical pressure would improve the contact between axons and electrodes, increasing the sealing resistance to the electrodes.

One possible scenario for the appearance of large axonal spikes in my recordings would be that cells, possibly astrocytes, are on top of the active axons, resulting in a similar increase in the sealing resistance. This hypothesis would also be in agreement with my own (**Figure 4-4**) and others (Lewandowska et al., 2015) results, in which small axonal spikes were observed below neuronal somas. If such a scenario is true, it can potentially lead to a 'contamination issue' when selecting electrodes close to visually-identified neuronal somata. The recorded activity might be originating from the soma or from the underlying axons, in the form of large axonal spikes. This could also explain some of the overlapping observed in my data.

If the presence of near-by cells affects the amplitude of axonal spikes, then axonal electrophysiology studies might be dependent on the culture conditions. For example, use of cytosine arabinoside for killing proliferating cells might also reduce the probability of observing large axonal spikes since there would be no non-neuronal cells to seal the axons. The benefit of using a protocol which promotes such recordings is in the higher signal-to-noise-ratio (SNR), which can aid in analyzing dynamic spike shape properties, such as the firing rate dependency used in this study. In combination with simultaneous somatic recordings, a procedure for differentiating between amplitude reduction and propagation failures can be implemented without the disadvantages of low SNR signals.

6.2. Axonal and somatic spike shape features

Comparison of the somatic and axonal spike shape features showed that the axonal spikes exhibit different features than somatic ones. Although some overlapping exists both the half-width and the trough-peak width values are smaller compared to the somatic spikes. I observed axonal bi-phasic, tri-phasic and spikes with a consistent double-negative-peak shape (**Figure 5-3**). A distinctive axonal spike shape was a symmetric, triphasic spike, denoted as Type 4 in my spike templates. Previous work has found that the spike shape could be used to distinguish excitatory from inhibitory neurons *in-vivo* (Barthó et al., 2004), but not *in-vitro* (Weir et al., 2015; Becchetti et al., 2012). Given such possible discrepancy, my findings highlight an important similarity between the *in-vivo* and *in-vitro* models. The observed different features could potentially allow researchers to filter them during data analysis, so that only the population of interest remains.

6.3. Evidence for axonal spikes recorded on MEAs

Previously, Ullo et al. (Ullo et al., 2014) used a similar approach as mine to study network properties at the mesoscale level, that of neuronal networks, at single-neuron resolution. The authors observed that electrodes with no nearby Neun+ neurons detected spiking activity. The source of this activity was hypothesized to be noise or electrical signals originating from strong dendritic arborization. I argue here that, besides noise and dendritic signals, another prominent source of activity on MEA recordings is active axonal segments.

My experiments with β3-tubulin staining and electrophysiological recordings showed extracellular activity originating both from neurites and somata. I classified these active neuritic segments as axonal segments, although β3-tubulin stains both dendrites and axons. A distinction between dendritic and axonal sources of activity could not be clearly performed, especially in footprints where the neuritic density was high (e.g.**Figure 5-2**). Regenerative dendritic activity, originating from dendritic Na^+, Ca^{2+}, or NMDA spikes, could indeed be included in my recordings (Spruston, 2008). Dendritic spikes are generally considered to exhibit strong amplitude attenuation with increasing distance, although this would not exclude detection at the site of dendritic spike initiation and it is an interesting mater of further investigation. However, the morphology of the highlighted neurite in **Figure 5-2** is more reminiscent of an axon, rather than a dendrite. In addition, a previous study using dissociated neurons on a HDMEA found minimum extracellular activity originating from the dendrite of a lipofected bipolar neuron (Bakkum et al., 2013).

Further analysis reinforces the argument that axons are responsible for the majority of the spikes recorded and analyzed in this work. The observed neuritic and somatic spikes I analyzed had one or more steep negative peaks of large amplitude. Such steep negative peaks do not appear in passive dendritic currents. Passive dendritic currents are usually composed of a large amplitude positive peak, followed by a shallow negative peak of small amplitude (Claverol-Tinture and Pine, 2002). In addition, the amplitude of dendritic regenerative APs depends on the firing history of the cell (Golding and Spruston, 1998), while the dendritic sodium channel inactivation properties are similar to the somatic ones (Mickus et al., 1999; Huguenard et al., 1989). Weak amplitude adaptation in the neuritic signals, as was observed in this work, argues against their classification as regenerative dendritic spikes. Furthermore, analysis of the spike shape indicated the presence of narrow, triphasic spikes, our Type 4 template, with a trough-peak width of 200 μs. Very similar spikes have been previously observed in white-matter areas of freely-behaving animals and classified as axonal spikes (Robbins et al., 2013).

The different spike shapes generated by dendrites, somata, and axons might be explained by the selective localization of potassium channels (Kv). Neuronal somata contain an abundance of Kv2, dendrites are composed of both Kv2 and Kv4.2, while axons mostly contain Kv1 and Kv7 channels (Jensen et al., 2011; Shibata et al., 2000; Rivera et al., 2007). The fast activation of Kv1.2 channels has been previously implicated in shaping the duration of axonal, but not somatic action potential (Shu et al., 2007b). Kv1.2 channels also exhibit slow inactivation which might explain the reduced adaptation rate of axonal spikes in my recordings (Shu et al., 2007b). Pharmacology studies could shed light on the relationship of axonal ion channels to network activity, for example by selective blockade of Kv1.2 and subsequent network-wide recordings.

6.4. Conclusions

To conclude, my findings indicate the presence of somatic and axonal spikes on HDMEA recordings. My work suggests that somatic and axonal origins of extracellular activity could be distinguished by spike shape features and/or their activity-dependency profiles. Further experiments are needed to drive the neurons to even higher firing frequencies and further support the axonal spike adaptation findings. It would also be interesting to see if the neurons can be

forced to switch mode, from one where axonal spikes are independent of the firing rate to a firing rate-dependent one, similar to the somatic spikes. Such studies will enhance our understanding of the relationship between single neurons and networks and they will further provide valuable information for neuroprosthetics (e.g. suitable stimulation patterns).

7. References

Anastassiou, C. a., Perin, R., Buzsaki, G., Markram, H., and Koch, C. (2015). *Cell-type- and activity-dependent extracellular correlates of intracellular spiking*. doi:10.1152/jn.00628.2014.

Bakkum, D. J., Frey, U., Radivojevic, M., Russell, T. L., Müller, J., Fiscella, M., Takahashi, H., and Hierlemann, A. (2013). Tracking axonal action potential propagation on a high-density microelectrode array across hundreds of sites. *Nat. Commun.* 4, 2181. doi:10.1038/ncomms3181.

Baltz, T., de Lima, A. D., and Voigt, T. (2010). Contribution of GABAergic interneurons to the development of spontaneous activity patterns in cultured neocortical networks. *Front. Cell. Neurosci.* 4, 15. doi:10.3389/fncel.2010.00015.

Barthó, P., Hirase, H., Monconduit, L., Zugaro, M., Harris, K. D., and Buzsáki, G. (2004). Characterization of neocortical principal cells and interneurons by network interactions and extracellular features. *J. Neurophysiol.* 92, 600–8. doi:10.1152/jn.01170.2003.

Bastmeyer, M., and O'Leary, D. D. (1996). Dynamics of target recognition by interstitial axon branching along developing cortical axons. *J. Neurosci.* 16, 1450–1459.

Becchetti, A., Gullo, F., Bruno, G., Dossi, E., Lecchi, M., and Wanke, E. (2012). Exact distinction of excitatory and inhibitory neurons in neural networks: a study with GFP-GAD67 neurons optically and electrophysiologically recognized on multielectrode arrays. *Front. Neural Circuits* 6, 63. doi:10.3389/fncir.2012.00063.

Beggs, J. M., and Plenz, D. (2003). Neuronal avalanches in neocortical circuits. *J. Neurosci.* 23, 11167–77. Available at: http://www.ncbi.nlm.nih.gov/pubmed/14657176.

Berdondini, L., Massobrio, P., Chiappalone, M., Tedesco, M., Imfeld, K., Maccione, A., Gandolfo, M., Koudelka-Hep, M., and Martinoia, S. (2009). Extracellular recordings from locally dense microelectrode arrays coupled to dissociated cortical cultures. *J. Neurosci. Methods* 177, 386–396. doi:10.1016/j.jneumeth.2008.10.032.

Blanche, T. J., and Swindale, N. V (2006). Nyquist interpolation improves neuron yield in multiunit recordings. *J. Neurosci. Methods* 155, 81–91. doi:10.1016/j.jneumeth.2005.12.031.

Chance, F. S., Abbott, L. F., and Reyes, A. D. (2002). Gain modulation from background synaptic input. *Neuron* 35, 773–782. doi:10.1016/S0896-6273(02)00820-6.

Chiappalone, M., Bove, M., Vato, A., Tedesco, M., and Martinoia, S. (2006). Dissociated cortical networks show spontaneously correlated activity patterns during in vitro development. *Brain Res.* 1093, 41–53. doi:10.1016/j.brainres.2006.03.049.

Chiappalone, M., Vato, A., Tedesco, M. B., Marcoli, M., Davide, F., and Martinoia, S. (2003). Networks of neurons coupled to microelectrode arrays: a neuronal sensory system for pharmacological applications. *Biosens. Bioelectron.* 18, 627–634.

Claverol-Tinture, E., and Pine, J. (2002). Extracellular potentials in low-density dissociated neuronal cultures. *J. Neurosci. Meth.* 117, 13–21.

Corner, M. a. (2008). Spontaneous neuronal burst discharges as dependent and independent variables in the maturation of cerebral cortex tissue cultured in vitro: A review of activity-dependent studies in live "model" systems for the development of intrinsically generated bioel. *Brain Res. Rev.* 59, 221–244. doi:10.1016/j.brainresrev.2008.08.001.

Czarnecki, A., Tscherter, A., and Streit, J. (2012). Network activity and spike discharge oscillations in cortical slice cultures from neonatal rat. *Eur. J. Neurosci.* 35, 375–388. doi:10.1111/j.1460-9568.2011.07966.x.

Debanne, D. (2004). Information processing in the axon. *Nat. Rev. Neurosci.* 5, 304–316. doi:10.1038/nrn1397.

Debanne, D., Campanac, E., Bialowas, A., Carlier, E., and Alcaraz, G. (2011). Axon physiology. *Physiol. Rev.* 91, 555–602. doi:10.1152/physrev.00048.2009.

Destexhe, a, and Paré, D. (1999). Impact of network activity on the integrative properties of neocortical pyramidal neurons in vivo. *J. Neurophysiol.* 81, 1531–1547.

Dworak, B. J., and Wheeler, B. C. (2009). Novel MEA platform with PDMS microtunnels enables the detection of action potential propagation from isolated axons in culture. *Lab Chip* 9, 404–10. doi:10.1039/b806689b.

Le Feber, J., Stegenga, J., and Rutten, W. L. C. (2010). The effect of slow electrical stimuli to achieve learning in cultured networks of rat cortical neurons. *PLoS One* 5, e8871. doi:10.1371/journal.pone.0008871.

Fiscella, M., Farrow, K., Jones, I. L., Jäckel, D., Müller, J., Frey, U., Bakkum, D. J., Hantz, P., Roska, B., and Hierlemann, A. (2012). Recording from defined populations of retinal ganglion cells using a high-density CMOS-integrated microelectrode array with real-time switchable electrode selection. *J. Neurosci. Methods* 211, 103–13. doi:10.1016/j.jneumeth.2012.08.017.

Fitzgerald, J. J., Lacour, S. P., McMahon, S. B., and Fawcett, J. W. (2008). Microchannels as axonal amplifiers. *IEEE Trans. Biomed. Eng.* 55, 1136–46. doi:10.1109/TBME.2007.909533.

Frey, U., Sedivy, J., Heer, F., Pedron, R., Ballini, M., Mueller, J., Bakkum, D., Hafizovic, S., Faraci, F. D., Greve, F., et al. (2010). Switch-Matrix-Based High-Density Microelectrode Array in CMOS Technology. *Solid-State Circuits, IEEE J.* 45, 467–482. doi:10.1109/JSSC.2009.2035196.

Furukawa, Y., Kasai, N., and Torimitsu, K. (2009). Effect of Mg2+ on neural activity of rat cortical and hippocampal neurons in vitro. *Magnes. Res.* 22, 174S–181S. Available at: http://www.ncbi.nlm.nih.gov/pubmed/19780405.

Geiger, R. P., and Jonas, P. (2000). Dynamic Control of Presynaptic Ca2+ Inflow by Fast-Inactivating K+ Channels in Hippocampal Mossy Fiber Boutons. *Neuron* 28, 927–939. doi:10.1016/S0896-6273(00)00164-1.

Golding, N. L., and Spruston, N. (1998). Dendritic sodium spikes are variable triggers of axonal action potentials in hippocampal CA1 pyramidal neurons. *Neuron* 21, 1189–1200. doi:10.1016/S0896-6273(00)80635-2.

Gritsun, T. a, le Feber, J., and Rutten, W. L. C. (2012). Growth dynamics explain the development of spatiotemporal burst activity of young cultured neuronal networks in detail. *PLoS One* 7, e43352. doi:10.1371/journal.pone.0043352.

Gross, G., Rieske, E., Kreutzberg, G., and Meyer, A. (1977). A new fixed-array multi-microelectrode system designed for long-term monitoring of extracellular single unit neuronal activity in vitro. *Neurosci. Lett.* 6, 101–105. Available at: http://linkinghub.elsevier.com/retrieve/pii/0304394077900039 [Accessed February 1, 2011].

Grossman, Y., Parnas, I., and Spira, M. E. (1979a). Differential conduction block in branches of a bifurcating axon. *J. Physiol.* 295, 283–305.

Grossman, Y., Parnas, I., and Spira, M. E. (1979b). Mechanisms involved in differential conduction of potentials at high frequency in a branching axon. *J. Physiol.* 295, 307–322.

Grubb, M. S., and Burrone, J. (2010). Activity-dependent relocation of the axon initial segment fine-tunes neuronal excitability. *Nature* 465, 1070–4. doi:10.1038/nature09160.

Henze, D. A., Borhegyi, Z., Csicsvari, J., Mamiya, A., Harris, K. D., and Buzsáki, G. (2000). Intracellular features predicted by extracellular recordings in the hippocampus in vivo. *J. Neurophysiol.* 84, 390–400. Available at: http://jn.physiology.org/cgi/content/abstract/84/1/390 [Accessed December 11, 2014].

Hill, D. N., Mehta, S. B., and Kleinfeld, D. (2011). Quality metrics to accompany spike sorting of extracellular signals. *J. Neurosci.* 31, 8699–705. doi:10.1523/JNEUROSCI.0971-11.2011.

Huguenard, J. R., Hamill, O. P., and Prince, D. a (1989). Sodium channels in dendrites of rat cortical pyramidal neurons. *Proc. Natl. Acad. Sci. U. S. A.* 86, 2473–2477.

Ito, D., Tamate, H., Nagayama, M., Uchida, T., Kudoh, S. N., and Gohara, K. (2010). Minimum neuron density for synchronized bursts in a rat cortical culture on multi-electrode arrays. *Neuroscience* 171, 50–61. doi:10.1016/j.neuroscience.2010.08.038.

Jäckel, D., Frey, U., Fiscella, M., Franke, F., and Hierlemann, A. (2012). Applicability of independent component analysis on high-density microelectrode array recordings. *J. Neurophysiol.* 108, 334–48. doi:10.1152/jn.01106.2011.

Jensen, C. S., Rasmussen, H. B., and Misonou, H. (2011). Neuronal trafficking of voltage-gated potassium channels. *Mol. Cell. Neurosci.* 48, 288–297. doi:10.1016/j.mcn.2011.05.007.

Kandel, E. R., Schwartz, J. H., and Jessell, T. M. (2000). *Principles of Neural Science*. doi:10.1036/0838577016.

Khodagholy, D., Gelinas, J. N., Thesen, T., Doyle, W., Devinsky, O., Malliaras, G. G., and Buzsáki, G. (2014). NeuroGrid : recording action potentials from the surface of the brain. *Nat. Neurosci.* doi:10.1038/nn.3905.

Kole, M. H. P., Ilschner, S. U., Kampa, B. M., Williams, S. R., Ruben, P. C., and Stuart, G. J. (2008). Action potential generation requires a high sodium channel density in the axon initial segment. *Nat. Neurosci.* 11, 178–186. doi:10.1038/nn2040.

Kole, M. H. P., Letzkus, J. J., and Stuart, G. J. (2007). Axon Initial Segment Kv1 Channels Control Axonal Action Potential Waveform and Synaptic Efficacy. *Neuron* 55, 633–647. doi:10.1016/j.neuron.2007.07.031.

Lago, N., Ceballos, D., J Rodríguez, F., Stieglitz, T., and Navarro, X. (2005). Long term assessment of axonal regeneration through polyimide regenerative electrodes to interface the peripheral nerve. *Biomaterials* 26, 2021–2031. doi:10.1016/j.biomaterials.2004.06.025.

Léger, J., Stern, E., Aertsen, A., and Heck, D. (2005). Synaptic integration in rat frontal cortex shaped by network activity. *J. Neurophysiol.* 93, 281–293. doi:10.1152/jn.00067.2003.

Lewandowska, M. K., Bakkum, D. J., Rompani, S. B., and Hierlemann, A. (2015). Recording Large Extracellular Spikes in Microchannels along Many Axonal Sites from Individual Neurons. *PLoS One* 10, e0118514. doi:10.1371/journal.pone.0118514.

Maccione, A., Benfenati, F., Berdondini, L., Gandolfo, M., Tedesco, M., Martinoia, S., Imfeld, K., and Koudelka-Hep, M. (2009). Imaging extracellular neuronal signaling on high resolution microelectrode arrays (MEAs): hippocampal cultures coupled with a high resolution neuroelectronic interface. *2009 4th Int. IEEE/EMBS Conf. Neural Eng. (NER 2009)*, 234–7|753. doi:10.1109/ner.2009.5109276.

Magee, J. C. (2000). Dendritic integration of excitatory synaptic input. *Nat. Rev. Neurosci.* 1, 181–190. doi:10.1038/35044552.

Meeks, J. P., Jiang, X., and Mennerick, S. (2005). Action potential fidelity during normal and epileptiform activity in paired soma-axon recordings from rat hippocampus. *J. Physiol.* 566, 425–441. doi:10.1113/jphysiol.2005.089086.

Meeks, J. P., and Mennerick, S. (2007). Action potential initiation and propagation in CA3 pyramidal axons. *J. Neurophysiol.* 97, 3460–3472. doi:10.1152/jn.01288.2006.

Mickus, T., Jung, H., and Spruston, N. (1999). Properties of Slow, Cumulative Sodium Channel Inactivation in Rat Hippocampal CA1 Pyramidal Neurons. 76, 846–860.

Monsivais, P., Clark, B. A., Roth, A., and Hausser, M. (2005). Determinants of action potential propagation in cerebellar Purkinje cell axons. *J Neurosci* 25, 464–472. Available at: http://eutils.ncbi.nlm.nih.gov/entrez/eutils/elink.fcgi?cmd=prlinks&dbfrom=pubmed&retmode=ref&id=15647490.

Müller, J., Ballini, M., Livi, P., Chen, Y., Radivojevic, M., Shadmani, A., Viswam, V., Jones, I. L., Fiscella, M., Diggelmann, R., et al. (2015). High-resolution CMOS MEA platform to study neurons at subcellular, cellular, and network levels. *Lab Chip*. doi:10.1039/C5LC00133A.

Nam, Y., and Wheeler, B. C. (2011). In vitro microelectrode array technology and neural recordings. *Crit. Rev. Biomed. Eng.* 39, 45–61. Available at: http://www.ncbi.nlm.nih.gov/pubmed/21488814.

Opitz, T., De Lima, A. D., and Voigt, T. (2002). Spontaneous development of synchronous oscillatory activity during maturation of cortical networks in vitro. *J. Neurophysiol.* 88, 2196–206. doi:10.1152/jn.00316.2002.

Pan, L., Alagapan, S., Franca, E., Demarse, T., Brewer, G. J., and Wheeler, B. C. (2014). Large extracellular spikes recordable from axons in microtunnels. *IEEE Trans. Neural Syst. Rehabil. Eng.* 22, 453–459. doi:10.1109/TNSRE.2013.2289911.

Paré, D., Shink, E., Gaudreau, H., Destexhe, a, and Lang, E. J. (1998). Impact of spontaneous synaptic activity on the resting properties of cat neocortical pyramidal neurons In vivo. *J. Neurophysiol.* 79, 1450–1460.

Park, J. W., Vahidi, B., Taylor, A. M., Rhee, S. W., and Jeon, N. L. (2006). Microfluidic culture platform for neuroscience research. *Nat. Protoc.* 1, 2128–36. doi:10.1038/nprot.2006.316.

Van Pelt, J., Corner, M. a, Wolters, P. S., Rutten, W. L. C., and Ramakers, G. J. a (2004). Longterm stability and developmental changes in spontaneous network burst firing patterns in dissociated rat cerebral cortex cell cultures on multielectrode arrays. *Neurosci. Lett.* 361, 86–9. doi:10.1016/j.neulet.2003.12.062.

Van Pelt, J., Vajda, I., Wolters, P. S., Corner, M. a, and Ramakers, G. J. a (2005). Dynamics and plasticity in developing neuronal networks in vitro. *Prog. Brain Res.* 147, 173–88. doi:10.1016/S0079-6123(04)47013-7.

Pine, J. (1980). Recording action potentials from cultured neurons with extracellular microcircuit electrodes. *J. Neurosci. Methods* 2, 19–31. Available at: http://linkinghub.elsevier.com/retrieve/pii/0165027080900424 [Accessed February 1, 2011].

Regehr, K. J., Domenech, M., Koepsel, J. T., Carver, K. C., Ellison-Zelski, S. J., Murphy, W. L., Schuler, L. a, Alarid, E. T., and Beebe, D. J. (2009). Biological implications of polydimethylsiloxane-based microfluidic cell culture. *Lab Chip* 9, 2132–2139. doi:10.1039/b903043c.

Rivera, J., Chu, P. J., Lewis, T. L., and Arnold, D. B. (2007). The role of Kif5B in axonal localization of Kv1 K+ channels. *Eur. J. Neurosci.* 25, 136–146. doi:10.1111/j.1460-9568.2006.05277.x.

Robbins, A. a, Fox, S. E., Holmes, G. L., Scott, R. C., and Barry, J. M. (2013). Short duration waveforms recorded extracellularly from freely moving rats are representative of axonal activity. *Front. Neural Circuits* 7, 181. doi:10.3389/fncir.2013.00181.

Scott, L. L., Hage, T. a, and Golding, N. L. (2007). Weak action potential backpropagation is associated with high-frequency axonal firing capability in principal neurons of the gerbil medial superior olive. *J. Physiol.* 583, 647–661. doi:10.1113/jphysiol.2007.136366.

Shibata, R., Nakahira, K., Shibasaki, K., Wakazono, Y., Imoto, K., and Ikenaka, K. (2000). A-type K+ current mediated by the Kv4 channel regulates the generation of action potential in developing cerebellar granule cells. *J. Neurosci.* 20, 4145–4155. doi:20/11/4145 [pii].

Shu, Y., Duque, A., Yu, Y., Haider, B., and McCormick, D. a (2007a). Properties of action-potential initiation in neocortical pyramidal cells: evidence from whole cell axon recordings. *J. Neurophysiol.* 97, 746–60. doi:10.1152/jn.00922.2006.

Shu, Y., Yu, Y., Yang, J., and McCormick, D. a (2007b). Selective control of cortical axonal spikes by a slowly inactivating K+ current. *Proc. Natl. Acad. Sci. U. S. A.* 104, 11453–11458. doi:10.1073/pnas.0702041104.

Spruston, N. (2008). Pyramidal neurons: dendritic structure and synaptic integration. *Nat. Rev. Neurosci.* 9, 206–21. doi:10.1038/nrn2286.

Srinivas, K. V, Jain, R., Saurav, S., and Sikdar, S. K. (2007). Small-world network topology of hippocampal neuronal network is lost, in an in vitro glutamate injury model of epilepsy. *Eur. J. Neurosci.* 25, 3276–86. doi:10.1111/j.1460-9568.2007.05559.x.

Stegenga, J., Le Feber, J., Marani, E., and Rutten, W. L. C. (2008). Analysis of cultured neuronal networks using intraburst firing characteristics. *IEEE Trans. Biomed. Eng.* 55, 1382–90. doi:10.1109/TBME.2007.913987.

Steriade, M. (2001). Impact of network activities on neuronal properties in corticothalamic systems. *J. Neurophysiol.* 86, 1–39.

Stratton, P., Cheung, A., Wiles, J., Kiyatkin, E., Sah, P., and Windels, F. (2012). Action potential waveform variability limits multi-unit separation in freely behaving rats. *PLoS One* 7. doi:10.1371/journal.pone.0038482.

Stutzki, H., Leibig, C., Andreadaki, A., Fischer, D., and Zeck, G. (2014). Inflammatory stimulation preserves physiological properties of retinal ganglion cells after optic nerve injury. *Front. Cell. Neurosci.* 8, 38. doi:10.3389/fncel.2014.00038.

Sun, J.-J., Kilb, W., and Luhmann, H. J. (2010). Self-organization of repetitive spike patterns in developing neuronal networks in vitro. *Eur. J. Neurosci.* 32, 1289–99. doi:10.1111/j.1460-9568.2010.07383.x.

Taylor, A. M., Blurton-Jones, M., Rhee, S. W., Cribbs, D. H., Cotman, C. W., and Jeon, N. L. (2005). A microfluidic culture platform for CNS axonal injury, regeneration and transport. *Nat. Methods* 2, 599–605. doi:10.1038/nmeth777.

Thomas, C. A., Springer, P. A., Loeb, G. E., Berwald-Netter, Y., and Okum, L. M. (1972). A miniature microelectrode array to monitor the bioelectric activity of cultured cells. *Exp. Cell Res.* 74, 61–66.

Ullo, S., Nieus, T. R., Sona, D., Maccione, A., Berdondini, L., and Murino, V. (2014). Functional connectivity estimation over large networks at cellular resolution based on electrophysiological recordings and structural prior. *Front. Neuroanat.* 8, 137. doi:10.3389/fnana.2014.00137.

Weihberger, O., Okujeni, S., Mikkonen, J. E., and Egert, U. (2013). Quantitative examination of stimulus-response relations in cortical networks in vitro. *J. Neurophysiol.* 109, 1764–74. doi:10.1152/jn.00481.2012.

Weir, K., Blanquie, O., Kilb, W., Luhmann, H. J., and Sinning, A. (2015). Comparison of spike parameters from optically identified GABAergic and glutamatergic neurons in sparse cortical cultures. *Front. Cell. Neurosci.* 8, 1–12. doi:10.3389/fncel.2014.00460.

Zeck, G., Lambacher, A., and Fromherz, P. (2011). Axonal transmission in the retina introduces a small dispersion of relative timing in the ganglion cell population response. *PLoS One* 6, e20810. doi:10.1371/journal.pone.0020810.

8. Supplementary Material

Table S1. Medium composition.

Name	Content	Supplier, Cat.No.
Dissection	HBSS without Ca2+ and Mg2+	Gibco, NO. 14175
Plating	Neurobasal A	Gibco, NO. 21103
	10% Fetal bovine serum	Gibco, NO. 10091
	2% B27 Supplement	Gibco, NO. 17504
	1:100 GlutaMax	Gibco, NO. 35050
	1:1000 Gentamicin (final 10µg/ml)	Sigma-Aldrich, NO. G1397
Culture	Nerve Culture Medium (NCM)*	Sumitomo, NO. MB-X9501

*Serum-free, Astrocyte conditioned medium based on DMEM/Hams's F12.

Table S2. Culture, immunostaining and somatic/axonal footprints selection details.

Culture	Plating		Days	Recording	Immunofluorescence	Footprints	
	No.	Density	in vitro	Time in min		Single Soma	Axons only
Culture-1	1	5,000 cells	25	1 min	β3-tubulin, DAPI	1	10
Culture - 2	2	10,000 cells	36	2 min	β3-tubulin, NeuN, DAPI	2	0
Culture - 3	2	10,000 cells	42	2 min	β3-tubulin, NeuN, DAPI	9	12
Culture - 4	3	10,000 cells	14	3 min	β3-tubulin, NeuN, DAPI	11	5
Culture - 5	3	10,000 cells	21	3 min	β3-tubulin, NeuN, DAPI	3	2
Culture - 6	2	10,000 cells	30	2 min	-	-	-
Culture - 7	4	10,000 cells	25	2 min	-	-	-
Culture - 8	4	10,000 cells	23	2 min	-	-	-
Culture - 9	4	10,000 cells	58	2 min	-	-	-
Culture - 10	4	10,000 cells	58	2 min	-	-	-
					Total	26	29
						55	

Table S3. Summary of spike sorted data. For each axonal or somatic footprint spike-sorting was performed. Most of the somatic footprints data resulted in a single cluster, with the exception of e.g. culture 3, in which somatic signals were usually accompanied by small neuritic spikes. Resulting somatic or axonal clusters also had minimum RPV, with an average of 0% over all somatic and 0.4% for the axonal footprints.

Culture	**Footprints containing a single cluster**		**Average RPV observed in the analyzed clusters**	
	% of somatic footprints	**% of axonal footprints**	**somatic footprints %**	**axonal footprints %**
Culture-1	100	80	0	0.4
Culture -2	100	-	0	-
Culture -3	20	100	0	1.2
Culture -4	70	100	0	0
Culture -5	100	100	0	0
Average	**78**	**95**	**0**	**0.4**

9. Author's previous academic achievements

9.1. Journal publications

M. E. J. Obien, K. Deligkaris, T. Bullmann, D. J. Bakkum, and U. Frey, "Revealing neuronal function through microelectrode array recordings," Front. Neurosci., vol. 8, no. 423, Jan. 2015

K. Deligkaris, T. S. Tadele, W. Olthuis, and A. van den Berg, "Hydrogel-based devices for biomedical applications," Sensors Actuators B Chem., vol. 147, no. 2, pp. 765–774, Jun. 2010.

K. V. Deligkaris, Z. D. Zaharis, D. G. Kampitaki, S. K. Goudos, I. T. Rekanos, and M. N. Spasos, "Thinned Planar Array Design Using Boolean PSO With Velocity Mutation," IEEE Trans. Magn., vol. 45, no. 3, pp. 1490–1493, Mar. 2009.

9.2. Talks and seminars

K. Deligkaris, "Separation of Single and Multi Neuronal Units in Low-Density Dissociated Cultures", 2nd Neuro CMOS Symposium, 20 January 2015, RIKEN Kobe, Kobe, Japan

K. Deligkaris, "Controlling GABAergic Composition and Identifying Local Properties in Networks of Dissociated Cortex", 1st Neuro CMOS Symposium, 20 May 2014, Research Center for Advanced Science and Technology, Tokyo, Japan

K. Deligkaris, "Investigating Neural Network Dynamics in-Vitro with a Focus on the GABAergic System", RIKEN CDB Luncheon Forum, 22 November 2013, Kobe, Japan

9.3. Conference poster contributions

K. Deligkaris, D. J. Bakkum, A. Hierlemann, and U. Frey, “Identification And Analysis Of Large Amplitude Axonal Spikes In Spontaneously-Active Neural Networks”, accepted in Neuro 2015, Kobe, Japan, 2015

K. Deligkaris, F. Gunneweg, D. J. Bakkum, A. Hierlemann, and U. Frey, “Mapping Extracellular Spike Shapes to Neuronal Location and Type: A Study with Microelectrode Arrays and Fluorescence Imaging,” in Neuro 2014, pp. P3–379, Yokohama, Japan, 2014.

K. Deligkaris, S. Kim, D. J. Bakkum, A. Hierlemann, and U. Frey, “Dynamics of Multiple Interconnected Neuronal Populations Cultured on a High-Density Microelectrode Array System,” in The 36th Annual Meeting of the Japan Neuroscience Society, Neuro2013, pp. P1–2–222, Kyoto, Japan, 2013.

K. Deligkaris, J. Kaneko, M. Fiscella, I. L. Jones, M. Engelene, A. Hierlemann, M. Takahashi, and U. Frey, “Detecting Light Response Patterns of rd1 Mouse Retinae: Electrophysiological and Optical Challenges,” in Proceedings of The Institute of Electrical Engineers of Japan Meeting, pp. 1747–1748, Hirosaki, Japan, 2012.

K. Deligkaris, J. Kaneko, M. Fiscella, J. Müller, I. L. Jones, A. Hierlemann, M. Takahashi, and U. Frey, “Light Response Patterns in Silenced rd1 Mouse Retinal Ganglion Cells,” in Proceedings of the 8th International Meeting on Substrate-Integrated Microelectrode Arrays, Reutlingen, Germany, 2012.

K. Deligkaris, J. Stegenga, and J. Feber, “Alcohol effects on cortical cultures,” in 7th International Meeting on Substrate-Integrated Micro Electrode Arrays, Reutlingen, Germany, 2010.

M. Spasos, N. Charalampidis L. Talbotier, J. Nanni, V. Beslouin, K. Deligkaris, “A novel design for an RF MEMS resistive switch on PCB substrate”, 2nd STIMESI workshop on MEMS and Microsystems Research and Teaching, Berlin, Germany, 2008.

K. Deligkaris, Z. Zaharis, D. Kampitaki, S. Goudos, I. Rekanos, M. Spasos, “Thinned Planar Array Design Using Boolean PSO with Velocity Mutation”, Thirteenth Biennial IEEE Conference on Electromagnetic Field Computation (CEFC 2008), Athens, Greece, 2008.